RICE UNIVERSITY

Magnetic Flux Leakage Robotic Pipe Inspection: Internal and External Methods

by

Andrew J. Lynch

A Thesis Submitted
in Partial Fulfillment of the
Requirements for the Degree

Master of Science

Approved, Thesis Committee:

Dr. Fathi H. Ghorbel, Chair
Professor of Mechanical Engineering and
Materials Science

Dr. Marcia K. O'Malley
Assistant Professor of Mechanical
Engineering and Materials Science

Dr. Andrew J. Dick
Assistant Professor of Mechanical
Engineering and Materials Science

Dr. Sushant M. Dutta
Scientist
Baker Hughes

Houston, Texas

December, 2009

Abstract

Magnetic Flux Leakage Robotic Pipe Inspection: Internal and External Methods

by

Andrew J. Lynch

Magnetic Flux Leakage (MFL) inspection generates a magnetic field through ferromagnetic materials and correlates anomalies in uniform field levels to defects in the structure. MFL has grown into a crucial method for inspection of pipelines and tubing in order to prevent long-term failures. Industry relies on MFL as a simple inspection indicator, but characterizing defects using MFL is an open research area. Numerous issues arise in MFL when the magnetic field does not radiate uniformly. For the framework of my thesis, I propose an experimental solenoid to control the field uniformity and enhance understanding of magnetic flux leakage calibration methods. This thesis delineates an analysis of the experimental solenoid and an in-depth verification of an internal pipe robot. The analysis compares internal and external inspection methods for magnetic flux leakage experiments.

Acknowledgements

I dedicate this work to my family and friends. Their patience has made my experience with Rice possible.

I also express many thanks to my advisor, Professor Fathi Ghorbel. His guidance and direction has been a strong influence in my writing and research.

Thank you to Dr. Dick and Dr. OMalley in their guidance on writing and presentation.

ItRobotics and employees Mr. Westlake, Dr. Jamoussi, Mr. Brusco and Dr. Wang have been a huge wealth of technical expertise for my work. I also want to thank the Rice technicians, Joe Gesenhues and Carlos Amaro for their assistance in construction and machining of parts.

Many thanks to my fellow graduate students Dr. Dutta, Mr. Landolsi and Mr. Chen. Dr. Dutta has been a close mentor throughout the entirety of my work. Mr. Landolsi has given me enthusiasm and motivation in times of need.

Many of the visiting students have been of great assistance in testing and implementation of the MFL research. Many thanks to Fabien Davos, Keila Fong, Ellen Farber, Megan Ruthven, Anthony Giovenal and Pierre-Phillipe Bonnefoy.

The Rice support staff has also been a huge assistance in writing, procedures and guidelines. Thank you to Aya Ossowski , Judith Farhat, Alicia Contreras and Dr. Janet Hewitt. Dr. Hewitt and her thesis writing course helped improve my writing skills tremendously.

Table of Contents

List of Figures

List of Tables

Chapter 1

Introduction

The petroleum industry is a major building block of the United States energy sector. Pipeline distribution and production are primary methods of transporting oil and natural gas. Improving pipeline technology with preventive maintenance is a challenging problem in the industry. Existing pipe infrastructure needs comprehensive inspection techniques to avoid catastrophic failures and serious environmental risks.

Detecting flaws in steel structures is a significant problem for society's infrastructure. Steel pipes are commonly used for transporting high pressure fluids. Coiled tubing (CT) is a widely used piping structure with unique bending characteristics. CT consists of a flexible steel pipe which is wound into a spool for rapid deployment as in Figure 1.1.

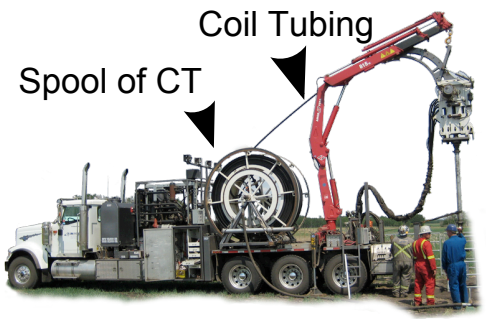

Figure 1.1: Coil Tubing Spool on Mobile Truck [1]

CT can vary from 0.75 to 4.5 diameter (inches) and maintain a continuous spool for over 30,000 feet [5]. Highly strained pipe has a tendency to produce more defects especially when pressurized. Fatigue due to repeated bending and spooling is the most common CT failure mode [6]. Coil tubing has grown into a viable alternative to conventional piping. The demand for high quality coil tubing inspection will grow as life expectancy of coil

tubing systems increase. Therefore, more accurate pipe inspection is becoming a highly requested technique to predict failures and improve lifetime of coiled steel tubing [7].

1.1 Background

Pipe inspection is crucial for manufacturing and preventive maintenance. Non destructive evaluation (NDE) techniques can span from electromagnetic, ultrasonic and radiographic. Inspection of pipeline using NDE techniques first started in the 1960s with Tuboscope [8]. The early methods of inspection involved high frequency ultrasonic signals to detect external cracks and defects. Small cracks and pits in pipeline wall can be caused by corrosion, bending stress and extreme temperatures. Ultrasonic inspection proved to be a complex forward modeling problem [3] and a challenging signal interpretation routine. In addition, ultrasonic inspection only detects outside surface defects and fails to sense the inner pipeline wall [9].

An electromagnetic inspection technique was proposed as an alternative to ultrasonic pipeline inspection in the 1970s [10]. The magnetic inspection process involves applying a magnetic field to a ferromagnetic structure and measuring the changes in magnetic flux density to determine the presence of a defect in the test specimen. Magnetic flux leakage is measured by Hall effect sensors. A Hall effect device produces voltage differences in a conductor with a changing electric current. The electric current is altered by a magnetic field oriented perpendicular to the conductor. In the pipeline inspection community, the technique of detecting ferromagnetic defects using magnetic fields is commonly referred to as magnetic flux leakage (MFL) inspection. The concept of MFL is easy to visualize in terms of flux lines moving through a pipe wall structure. The size of the defect varies the magnetic flux leakage into the surrounding air as depicted in Figure 1.2. One of the largest advantages of MFL inspection is the ability to detect internal pipe wall defects without line of sight. Acoustic, visual inspection and lasers are not sufficient for detecting cracks without surface scans of the material. Radiographic, eddy currents and MFL are potential

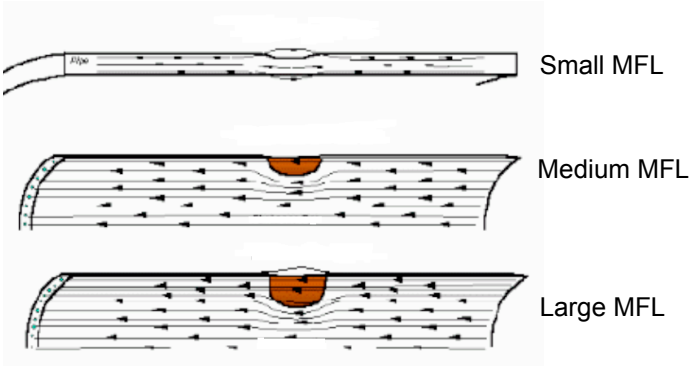

Figure 1.2: Magnetic flux leakage for different defect sizes[2]

methods of detecting internal cracks and corrosion inside a tubular pipe. Each of these methods can be oriented internally or external to the pipe wall. With low sensor costs and small space requirements, MFL inspection has become a leading inspection technique for the energy pipeline industry [5].

1.2 MFL Methods

The process of identifying defect characteristics from changes in a magnetic flux leakage signal is typically referred to as an inverse problem. Inverse problems in MFL rely heavily on previously generated calibration curves of defect geometry [11]. A more generalized modeling approach to MFL defect characterization has been presented in the literature [3]. Modeling MFL is a significant problem due to changes in field uniformity, relative permeability of test materials and external environment conditions. The differences in MFL inspection tools also present an interesting modeling constraint for the magnetic flux leakage problem. MFL inspection devices generally inspect pipes of small diameter (Table 1.1) using an externally applied field on the pipe wall [8]. These external MFL tools are built to generate a magnetic field using an electromagnet such as a solenoid or Helmholtz coil layout. The experiments in this work will mainly focus on a 2.5 inch inner diameter steel pipe.

Type	Outer Diameter	Inner Diameter	Wall Thickness	Torsional Yield Strength (lb/ft)
QT-1000	1.00	0.75	0.125	650
QT-1000	2.875	2.525	0.175	7450
QT-1000	3.5	3.150	0.175	13930

Table 1.1: Coiled Tubing Pipeline Dimensions (inches) [4]

Most external inspection devices include a solenoid and Hall effect measurement system for defect detection. The existing industry in nondestructive evaluation has a meager commercial interest in defect characterization due to the complex nature of the problem. Therefore, most pipeline inspection tools typically identify pipes that need to be replaced and do not dwell on the characteristics or severity of the defect. External inspection devices are not practical for installed pipeline in tight dimension constraints. The need for improved inspection devices is still a pressing issue in the non destructive evaluation field [12]. Recent developments in industry have presented internal inspection tools for small diameter pipe such as coil tubing and small pipelines. Internal MFL tools use permanent magnets to generate a uniform field at the inspection point of interest. Internal inspection devices are designed to accommodate one dimension of pipe with tolerance for small burrs and flash lines from welding. Comparing performance and experiments from internal and external pipe inspections improves MFL models and provides unique insight into optimal MFL design.

1.3 Pipe Wall Defects

Common defects on the outer pipe wall result from mechanical damage or environmental conditions. Defects such as corrosion create a wall-thinning effect as material is removed from the pipe wall. Other defects, possibly resulting from excessive stress or bending of the pipe, include holes, cracks and gouges [13]. Wall thinning is used as the most general

representation of a defect. For the purposes of this thesis, wall thinning defects are the primary defect considered. The pipeline being inspected is subjected to a magnetic field. Defects are essentially gaps in the pipe wall which lead to leakage of the magnetic flux density. Figure 1.3 illustrates the concepts of MFL signals produced by pipe wall defects. The radial and axial signal components will be discussed in section 4.1.2.

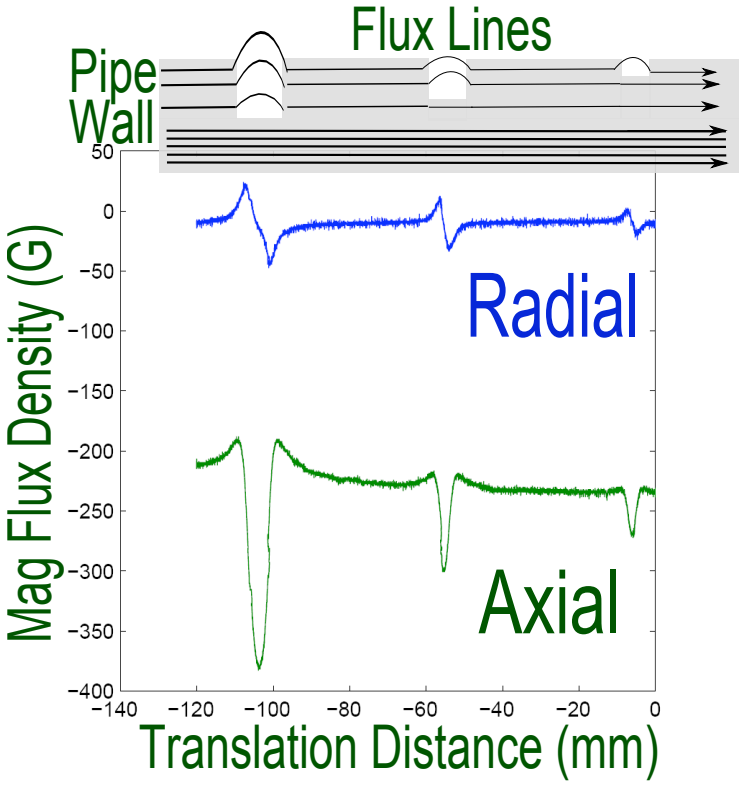

Figure 1.3: MFL Signals from small wall thinning defects

To properly characterize wall thinning defects, the internal inspection system uses MFL sensors. The MFL signal amplitude and curvature is dependent upon the volume of the defect. The MFL volume correlation is used to classify defects based on their signals. In order to expand the knowledge of the signals produced by different types of defects and different testing conditions, both experimental and simulated tests have been conducted [13, 14, 15, 16, 17].

1.4 Problem and Outline

The primary focus of the present work is to characterize experimental comparisons between internal and external inspection methods for magnetic flux leakage robots. In a non-destructive evaluation (NDE) of a ferromagnetic pipeline, a smart internal or external solenoid robot measures magnetic flux leakage while traversing the length of the pipe. The concept of NDE testing and MFL inspection is used throughout the thesis with special focus on design techniques and signal characterization.

1. The first part of the problem is to detail the inner workings of MFL robotic inspection process.

2. Perform comparison experiments to find intersections between internal and external inspection methods.

3. Analyze performance metrics and describe ideal design parameters for each type of MFL robotic inspection.

This thesis is organized as follows: In Chapter 2, the internal inspection technique is described with emphasize on sensor design and magnetizing configuration. The external solenoid coil inspection set-up is introduced in Chapter 3. The solenoid coil's geometry and the design constraints are presented along with uniformity and performance curves. Chapter 4 delineates the internal and external experiments with comparisons of performance metrics. Conclusions are provided in Chapter 5 including future directions for improving MFL-based inspection techniques.

1.5 Contributions

The previous background section covered MFL inspection methods and wall thinning defects. This section is focused on the issues and unique elements in MFL inspection techniques and signal analysis. The primary magnetic flux leakage inspection contributions

revolve around experimentation and analysis.

1. The first contribution is to provide insight into internal inspection process with a developed robotic inspection device. An overview of the device and detailed walk-through of internal inspection design is addressed in Chapter 2. Experiments and processed data are presented to provide a foundation for internal sensing data analysis.

2. This work outlines comparisons between internal and external MFL inspection methods with experimentation in Chapter 4. The experiment process is presented around a similar test material and equivalent defect characteristics. An analysis of MFL signals is presented in Chapter 5.

3. The external solenoid device developed is a unique approach to the field of MFL inspection. The split solenoid designed has well developed uniformity region with efficient power and dimension characteristics. The solenoid apparatus is well suited for validation of theoretical simplified MFL Models.

Chapter 2

Internal Inspection

Internal inspection involves collecting information about a tubular specimen from sensors inside the object. For the purpose of the present work, my thesis focuses on steel pipes with a mobile robot traversing inside of the pipe. Non-destructive evaluation is the preferred and most cost-effective method of pipe evaluation. The internal robot is equipped with fixed permanent magnets and Hall effect sensors for MFL measurements. The fixed magnets will form a closed magnetic circuit with the pipe wall for MFL sensor measurement. The internal robot inspection system has the ability to characterize pipe wall defects at any orientation. This section discusses internal inspection methodology and specific features of a commercial internal robotic system.

2.1 MFL Internal Robot

Internal inspection robots typically have self-contained sensor logging capabilities with complimentary battery power source. MFL internal robots' magnetic field must have sufficient strength to saturate the pipe wall. Figure 2.1 depicts an internal MFL Robot from itRobotics [3] also known as the Pipeline Coiled Tubing Inspector (PCTI 2.5).

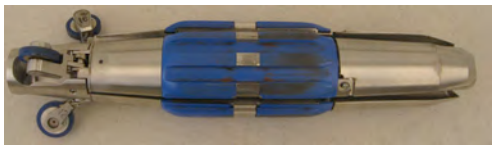

Figure 2.1: PCTI 2.5 Internal Robot from itRobotics

The PCTI 2.5 has undergone significant field tests and is designed for industry pipeline

inspection guage(PIG) usage. PIGs perform measurement operations without impeding the flow of the pipeline fluid. For most NDE applications, PIG inspection have significant economical benefits over actuated devices for corrosion metal loss in petroleum pipelines [18]. The PCTI is designed to navigate through 2.5" inner diameter pipe with a 0.5" tolerance for the flashline of the pipe. In most steel pipe construction, the flashline refers to the welding seam created when a sheet of steel is rolled into a tubular structure by welding (see Figure 2.2).

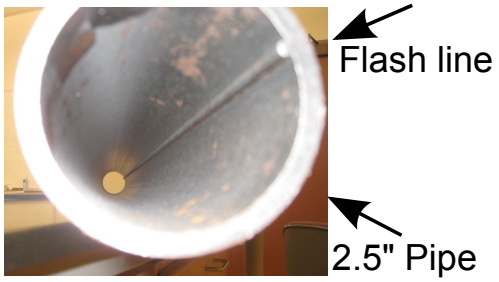

Figure 2.2: Flashline of 2.5" Pipe

2.1.1 Hall Effect Sensor

In the case of magnetic flux leakage pipe inspection, magnetic flux density is the most important quantity to measure. A Hall effect sensor is a suitable device for measuring changes in Magnetic Flux Density. The robot is outfitted with a dual-axis Hall effect sensors for measuring the axial and radial magnetic flux density (Figure 2.3).

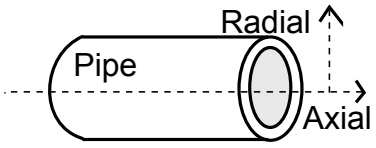

Figure 2.3: Radial and axial coordinates of pipe domain

As the robot moves over a defect, the Hall effect sensor detects changes in magnetic flux density. For proper detection of wall thinning defects, the sensor must have a near

millimeter lift-off from the defected specimen [3]. Lift-off is the distance between the sensor face and the surface of the object defined in Figure 2.4. Slight changes in Lift-off alter results drastically. The internal robot has permanent magnets constantly drawing

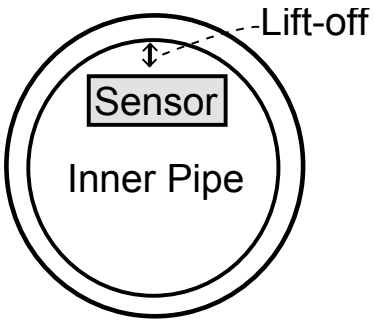

Figure 2.4: Internal Lift-off diagram

the robot to the internal wall of the pipe. The Hall effect sensor is located in between two permanent magnets. The sensor's position or lift-off from the pipe-wall remains constant. The robot traverses down the pipe while collecting odometry and sensor measurements into a single data scan log. Traversing a pipe with only one Hall effect sensor records a linear scan of the pipe. The robot also has rotation measurement capability to record orientation of the robot during traversal. To cover the surface area of the pipe, the robot is outfitted with nine different Hall effect sensor elements placed in a ring around the mid-section of the robot as in Figure 2.5.

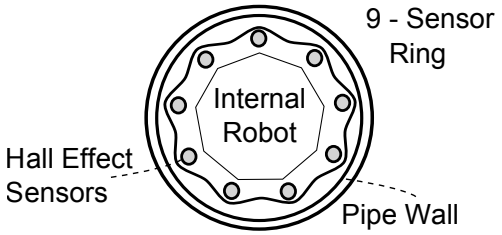

Figure 2.5: Ring of Hall Effect Sensors for Internal MFL Robot

2.1.2 Wedge Sections

The robot is divided into three sections called wedges as shown in Figure 2.6. Each wedge has its own self-sufficient data collection unit independent of the other wedges. The

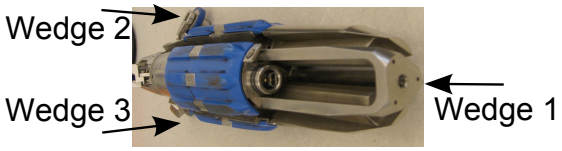

Figure 2.6: PCTI Internal Robot has three independent wedges

wedges log data based on encoder wheel measurements or logging at every time sample. Time based recording relies on measuring Hall effect signals at regular time interrupts on the micro-controller. Encoder based recording logs MFL sensor measurements based on distance tick marks. The robot's encoder is a torsion spring loaded mechanism that applies constant pressure to the pipe's internal wall, see Figure 2.7. The robot is moving at a constant velocity through the pipe and should produce similar encoder and time logs. The encoder based logging is ideal for data collection to factor out changes in robot velocity. For the series of experimental tests, the data is based off distance-encoder wheel recordings. Each wedge is configured to record axial and radial magnetic flux densities.

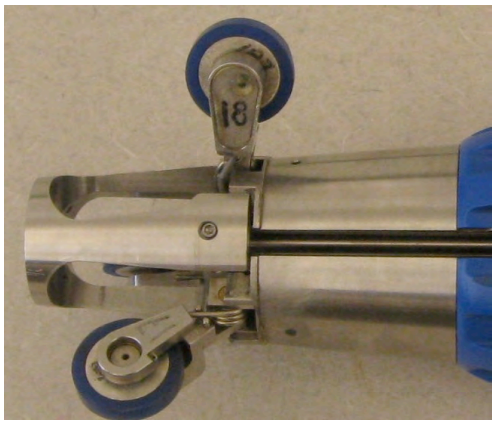

Figure 2.7: Encoder close-up on PCTI Internal MFL Robot

Changes in magnetic flux densities indicate pipe defects in the region of each sensor's

wedge. Depending on the geometry of the defect, defects can potentially overlap onto different sensor measurements. Defect overlap is ignored when measuring changes in wall thinning defects. The robot's permanent magnet is designed to close a magnetic circuit between the pipe wall and two opposite polarity magnets. A 3D layout of the PCTI Internal Robot from itRobotics [3] is shown in Figure 2.8. The ring of 9 dual axis Hall effect sensor is shown in green.

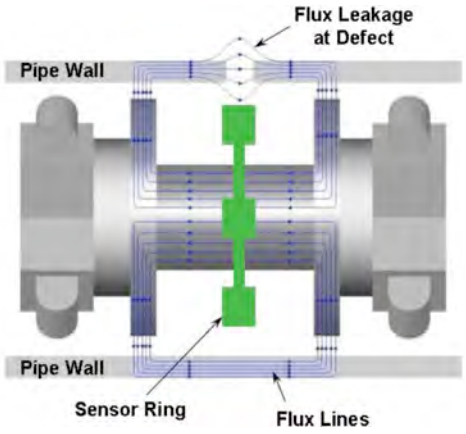

Figure 2.8: 3D Drawing of Internal MFL Robot [3].

The internal MFL field generation is broken into two radial magnets and a ferromagnetic core. The magnetizing field starts on a radially north polarized magnet. As depicted in Figure 2.9, the flow continues through the pipe wall until reaching the radially south polarized magnet (opposite). The ferromagnetic core is situated between the two magnets to maintain the strength of the field and reduce the size of the permanent magnetic material.

When the robot is inside the pipe the ferromagnetic wall is saturated locally between the robot's permanent magnets. When wall thinning or gaps in steel pipe occur, the magnetic flux density reading increases from the baseline saturation level [19]. The amplitude of the increase is related to the size of the wall thickness.

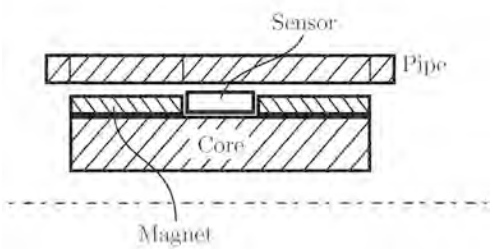

Figure 2.9: 2D Layout of Internal Robot MFL Components [3].

2.2 MFL Internal Robot Context

For internal pipe inspection, a series of tests were performed with an internal MFL robot and various segments of steel pipe. The robot traverses at a constant velocity and collects MFL sensor data and logs wheel encoder measurements. The sensor logs are later characterized in post-processing after the robot has exited the pipe. Defects are later characterized with an automated locating script. With sufficient experiment tests, the defect size data points produce an inverse identification model. The inverse model can be expanded to predict a large subset of potential pipe wall defects. The wall thinning model also provides a baseline for comparing the performance of internal and external inspection techniques.

Chapter 3

External Inspection

External MFL inspection requires the magnetic flux measurements to be taken outside of the test material. Similar to internal inspection, a magnetic field is generated to flow through the pipe. In the case of external pipe inspection, an electromagnetic solenoid coil generates a magnetic field through the pipe. When a pipe defect is present, the external sensor monitors variations in the magnetic flux density signals as shown in Figure 3.1. The variations increase with the defect's cross sectional area. External inspection platforms allow for more control of magnetic field characteristics than the internal robot's permanent magnets.

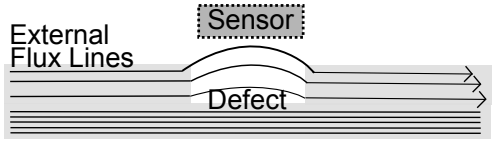

Figure 3.1: Hall-effect sensor measuring magnetic flux leakage from pipe defect.

3.1 External Solenoid Design

External MFL inspection consists of placing the a hall-effect sensor outside of the ferromagnetic test specimen. A field is radiated encompassing the sensor and the portion of the test material. In the case of external Solenoid coil inspection, the pipe is located concentric with the solenoid coils as in Figure 3.2. The hall-effect sensor is situated between the outside of the wall of the pipe and the inside wall of the solenoid.

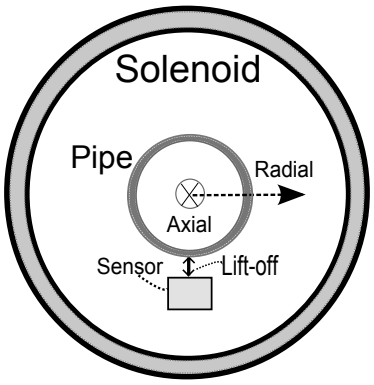

Figure 3.2: External MFL sensing layout with solenoid surrounding the pipe and sensor

Our robotic internal inspection involved a permanent magnet generating a constant magnetic field inside of the pipe. External magnetic field generation is typically produced through an electromagnetic solenoid or Helmholtz coils. Since the field is time-varying according to the power supplied and thermal characteristics of the system, the external magnetic field has more system parameters than a fixed-permanent magnet internal system. External inspection allows for the solenoid's magnetic field characteristics to be modified according to the input current density and solenoid dimensions. For the case of these MFL experiments, the solenoid is typically oriented outside the pipe specimen with field generation concentrating near the center of the coil axis as depicted in Figure 3.3.

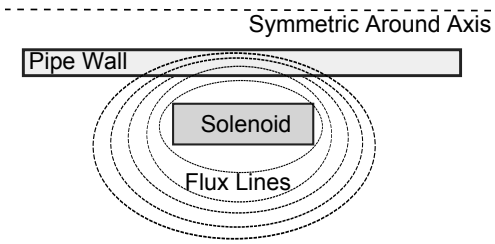

Figure 3.3: Projection of Solenoid Flux Lines around Pipe.

3.1.1 Magnetic Field Generation

Magnetic flux is the magnetic charge carried by closed magnetic field lines. Magnetic flux density B is given in units of Gauss (G) or Tesla ($1T = 10^4G$). Typically, magnetic field

levels are provided in terms of field strength or intensity(H) in units of Oersted. Magnetic flux density and intensity are related by the permeability of the magnetized medium.

$$B = \mu H \tag{3.1}$$

Magnetic permeability μ represents the relation between flux density and field intensity. Permeability is measure of magnetic flux diffusing or permeating a material in a given magnetic field [20]. Permeability varies across many types of materials. Free space permeability in air is μ_0=$4\pi \times 10^{-7}$.

MFL external inspection is focused on electromagnetic solenoid coils carrying current to produce a magnetic field. Visualization of a single wire generating a magnetic field is shown in Figure 3.4. The current direction determines the polarity of the magnetic field by the right-hand rule.

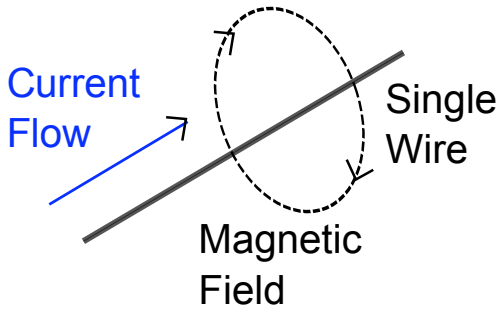

Figure 3.4: Single wire producing Magnetic Field

For a solenoid coil with multiple loops of wire, the coil's field strength H_{coil} can be related in terms of equation 3.2.

$$H_{coil} = NI_{apprx}/L \tag{3.2}$$

Where I_{apprx} is the approximate current going through the solenoid and N is the number of coils while L is the inductance of the coil.

The flux of the solenoid tends to space out tremendously and pack around the longitudinal field along the axis. Introducing a ferromagnetic object in the core of the solenoid

magnetizes the material. Flux leakage from the material occurs due to a reduction of flux flow area especially around a change of cross sectional area in the structure. The flux leakage varies depending on the object's magnetic permeability and the characteristics of the field.

3.1.2 Solenoid Physics

A solenoid produces a uniform magnetic field along the core axis and the field is weak outside the core. The number of flux lines in Figure 3.5 illustrate the magnetic flux density concentration of the field.

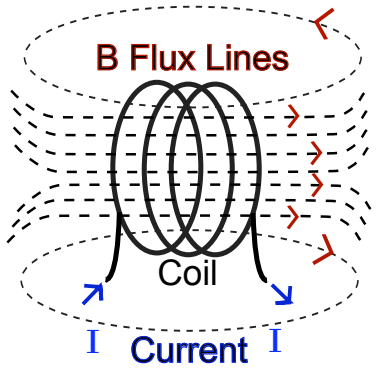

Figure 3.5: Aerial Projection of Solenoid Flux Lines.

For simplicity of analysis, the sum of all currents through a solenoid is lumped together as I_s. The free space permeability is assumed as μ_0.

- I_S - Sum of all Currents
- μ_0 - Free space permeability
- B_{ax} - Axial Magnetic Flux Density

The magnetic flux density along the axis of the solenoid is labeled B_{ax}. The axial magnetic flux density is related to the sum of currents flowing through the coil through magnetic

permeability as shown in Equation 3.3. B_{ax} is an ideal representation of core axial magnetic flux density in a open-air electromagnetic solenoid.

$$\oint \vec{B_{ax}} \vec{dl} = \mu_0 I_S \tag{3.3}$$

Solenoids are composed of a series of windings wrapped in different geometric patterns. The changes in windings alter volume of the generated magnetic field. The series of windings also affect heat dissipation, current density limitations, wire gauge and coil dimensions. Analysis of the solenoid windings divide into axial and radial winding turns as n_{ax} and n_{rad} respectively in Figure 3.6.

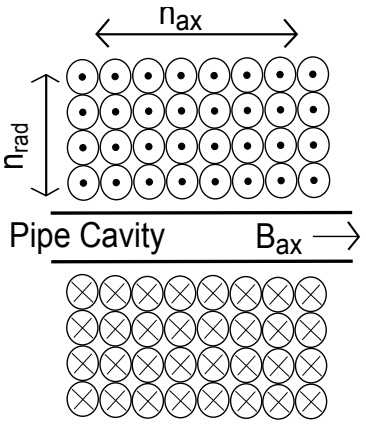

Figure 3.6: Coil Geometry of Multi-Coil Solenoid

We apply the following equation on the coil geometry in Figure 3.6 to obtain a B_{ax} field at the center of the solenoid's core as shown in equation 3.4. Where N is the total number of turns in the coil and L is the axial length of the solenoid coil.

$$B_{ax} = \mu_0 \frac{N I_S}{L} \tag{3.4}$$

The approximation of B_{ax} is helpful for overall field strength but does not consider field uniformity or saturation of the ferromagnetic test material. Table 3.1 indicates the split-solenoid coil's core dimensions to attain an adequate magnetic field strength for saturation and to obtain a uniformity region suitable for MFL experimentation.

Parameter	Description
$a_0 = 9$	coil inner diameter [inches]
$OD = 10.4$	coil outer diameter [inches]
$L = 4.2$	coil length [inches]
$d = 0.1716$	6 awg wire diameter - square copper [inches]
$n_{rad} = 4$	number of turns in radial direction
$n_{ax} = 24$	number of turns in axial direction
$n = 96$	number of total turns

Table 3.1: Dimension Parameters for Solenoid

3.1.3 Saturation

Saturation is an important concept in external MFL robot inspection [3]. Steel pipes and other soft ferromagnetic materials attract the majority of the magnetic flux from an externally generated field. The property of attracting magnetic flux can be referred to as magnetic permeability of the material. The permeability of the material varies according to the material and field applied to the material as shown in Figure 3.7. The curve at the top is a $B - H$ curve where B is the magnetic flux density and H is the applied magnetic field strength. The gray region in Figure 3.7 with larger values of H is referred to as the saturation region. The first non-saturation region depicts B with a sharp increase at low H fields. The knee of the $B - H$ curve separates the saturation region. Figure 3.7 shows a $\mu_r - H$ curve as a relationship between relative permeability variations at different magnetic field intensities. Similar to the B field, the μ_r values saturate near a constant value in the saturation region. When a defect decreases the pipe's volume, the near-constant relative permeability allows the magnetic flux to leak out of the pipe. Flux leakage measurements are difficult to detect if the field does not saturate the pipe wall. Therefore, the external solenoid saturates a ferro-magnetic pipe by attaining a moderately high H field. The saturation enables magnetic flux leakage to occur on defects.

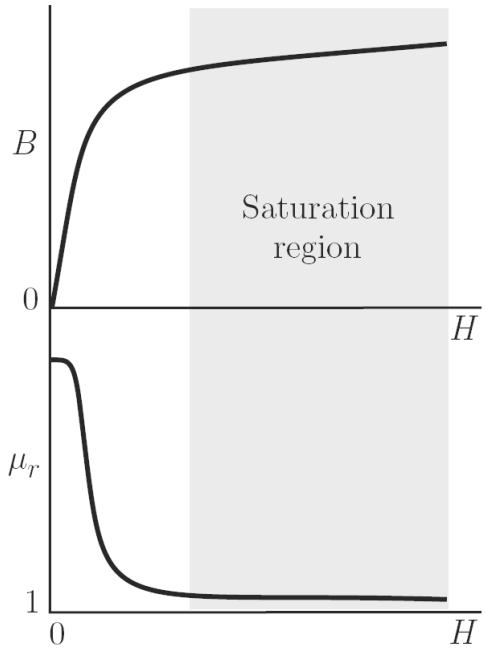

Figure 3.7: BH Properties of soft ferromagnetic material(pipe) [3] .

3.1.4 Uniformity

The applied magnetic field must reach the saturation point over a uniform region. A sufficient region insures the defect is uniformly magnetized and the relative permeability can be assumed to be locally constant based off the assumptions from Edwards [22]. In the external pipe inspection experiments, a solenoid provides a near-uniform cylindrical region of magnetic field around the test object. The uniformity of the field ensures that the magnetic flux density is radiated evenly around the outer surface of the pipe. The uniformity of the solenoid field can be modeled through elliptical integrals [23]. In the analysis of a solenoid coil, the uniformity of the axial and radial dimensions were simulated to produce Figure 3.8 uniformity cross-sections.

The uniformity of the solenoid coil declines gradually over axial distance changes as shown in Figure 3.8(a). The axial distance measurements are traversing along the axis of the solenoid's core. The radial uniformity plot in Figure 3.8(b) is exhibiting a significant drop in magnetic flux density. The drop occurs at the physical radius dimensions of the

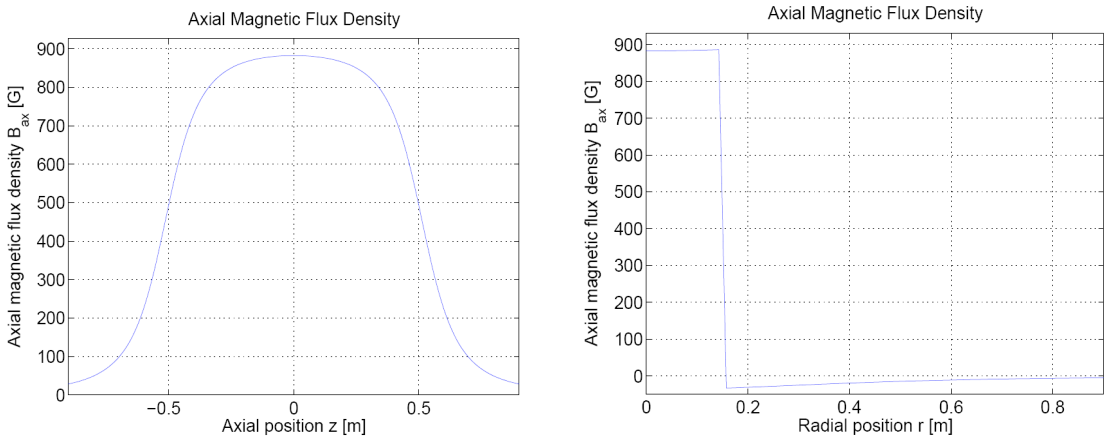

(a) B_{axial} versus Axial Distances

(b) B_{axial} versus Radial Distances

Figure 3.8: Axial Magnetic Flux Density versus Axial and Radial Distances

solenoid coil. The magnetic flux density is low on the outside of the solenoid coil.

3.1.5 Solenoid versus Helmholtz Coils

A solenoid coil or Helmholtz coil geometry is typically employed to generate a near-uniform magnetic field. A detailed comparison of the two external field generation methods was considered to select an ideal coil geometry. The goal in the analysis was to produce a time-varying uniform magnetic field in a cylindrical volumetric region. The region would encompass the hall-effect sensor and full pipe over a 1.5 inch length. The field generating coil also must produce a 450 Gauss field to saturate a coil tubing CT-90 material.
In the external field generation analysis, the axial magnetic flux densities were compared in simulation to gain insight about the uniformity region. Figure 3.9 illustrates the differences in uniformity region over the radial and axial dimensions. Both electromagnetic geometries show promising uniformity results for the region of interest.

The dimensions of the two coil geometries turned out to be a deciding factor for practical implementation. The solenoid coil would require a smaller volume of 1 foot cubed. The Helmholtz coil's simulated geometry was approaching a 2 foot cube with almost twice

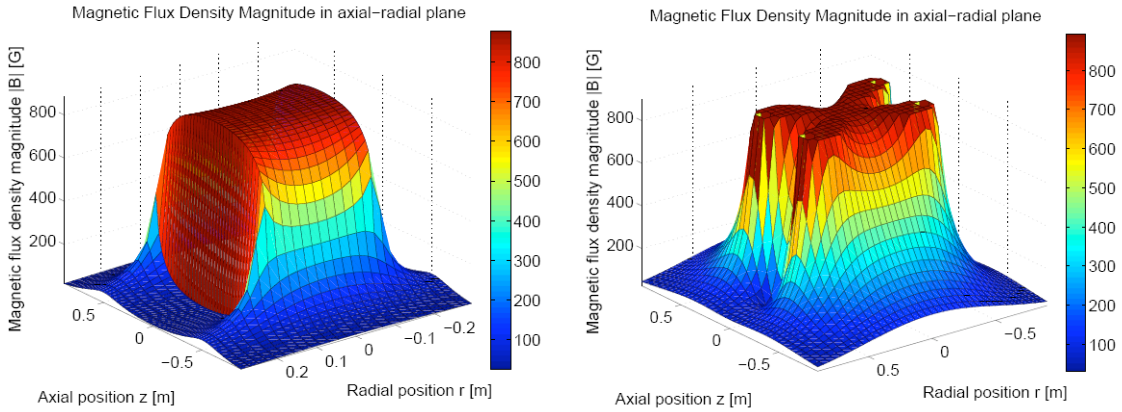

(a) Region of interest - Solenoid Coil

(b) Region of interest - Helmholtz Coil

Figure 3.9: Magnetic Flux Density comparison for Solenoid and Helmholtz Coils

the volume of the solenoid coil.

3.2 External MFL Inspection

The external inspection system consists of a solenoid, automated motion system, pipe-support and hall-effect sensors. The system is capable of detecting defects in four foot pipe sections. This section outlines the physical solenoid parameters , the motion system and the sensor specifications.

3.2.1 Solenoid Parameters

The solenoid was designed for attaining magnetic saturation levels for a 0.75-4" diameter (inches) pipe in accordance with the most common CT pipes (See Section 1.1). To reach saturation, the magnetic flux density B must reach at least 450 Gauss. The magnetic flux density can also exceed 450 Gauss without significant changes in MFL sensor calibration routines. In terms of safety, operating above 450 Gauss is dangerous due to the high current draw and heat generated. In order to calculate the field strength of a solenoid, the number of turns, current draw, coil radius and wire diameter combine into a single field

equation. A simplified solenoid model is first considered to transition to a more detailed model. The uniform magnetic flux density equation and voltage from a inductive circuit are provided in Equation 3.5.

$$B_{ax} = \mu_0 n_{ax} n_{rad} I_{appx} \tag{3.5}$$

$$V_{sol} = RI_{appx} + L\frac{dI_{appx}}{dt} \tag{3.6}$$

As an approximation of the magnetic flux density, one can substitute equation parameters from Tables 3.2 and 3.1 to compute the field strength.

Parameter	Description
$G = 452.359$	Central Field
$I_{appx} = 71.260$	current in the coil [amps]
$a_0 = 9$	coil diameter [inches]
$R = 0.1625$	resistance of coil [ohms]
$I_l = 5.477$	inductance of coil [mH]
$V = 11.577$	voltage of solenoid [V]

Table 3.2: Electrical Parameters for Solenoid

The physical solenoid was built by Walker Scientific according to the general specifications stated in Table 3.2 with water coolant hoses and coils integrated into a black plastic housing. The solenoid housing case is in a cube shape of 12.5"x12"x11.5" dimensions with a 9" diameter opening. The solenoid is mounted on a linear slide table as part of the automated inspection platform as shown in Figure 3.10.

The uniformity of the field only occurs in a cylindrical region situated in the center of the coil. The uniformity volume is important to achieve consistent magnetic flux density measurements for various diameter pipes. The uniformity volume dimensions in Table 3.3 show a field strength peak at the center of the coil. The uniformity from the peak field strength is approximately 0.825% or threshold U (Table 3.3) over the volumetric region centered in the coil.

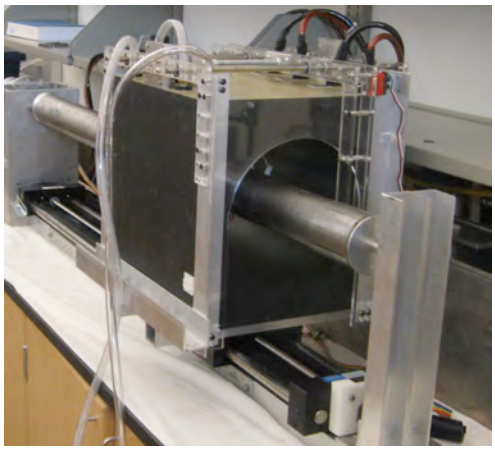

Figure 3.10: External Solenoid MFL Robotic Inspection Tool

Parameter	Description
$G = 452.359$	Central Field
$U = 0.825\%$	Uniformity
$U_{length} = 1.6$	Uniform Cylinder Length [inches]
$U_{diameter} = 4.0$	Uniform Cylinder Diameter [inches]

Table 3.3: Uniformity Parameters for Solenoid

3.2.2 Inspection System

The solenoid produces a 450 Gauss magnetic field to saturate a 1-4" ferrous pipe. To achieve 450 gauss, the solenoid operates at 5 volts and 78 amps from a 2000 watt power supply from AEHR power supply. The voltage number is different from previous estimates based on wire resistance from 7 foot long (4AWG) conductor cables. A complete surface scan of a pipe is needed to evaluate defects. Therefore, the pipe rotates while the solenoid translates along the pipe axis to perform a surface scan. The solenoid translates on a linear slide table by a stepper motor with a 50:1 harmonic gearbox. The pipe is rotated independently of the linear motion with an additional stepper-harmonic drive as shown in Figure 3.11. The inspection system has a translation resolution of 0.127 millimeter and a rotation resolution of 0.036 degrees.

Figure 3.11: External Solenoid MFL Power Components and System Diagram

A dual-axis hall effect sensor measures the radial and axial components of the magnetic flux density. The hall effect sensor is attached at the axial center of the 9" solenoid. The sensor enclosure provides a constant lift-off from the pipe wall. However the sensor's lift-off can be adjusted by a third stepper motor to perform automated lift-off measurements as shown in Figure 3.12. The lift-off stepper motor moves an acrylic yoke with the hall-effect sensor attached inside the core of the solenoid. The rigid sensor mounting structure traverses along a lead-screw with two steel supporting sliding rods. An encoder is mounted to the opposite side of the lead-screw to allow for precision data collection of lift-off movements.

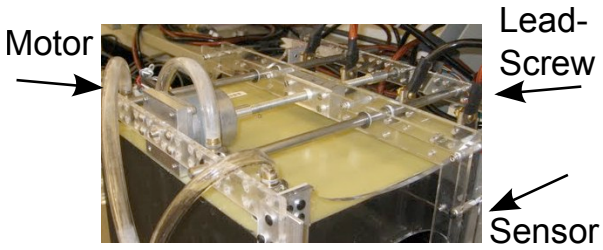

Figure 3.12: Motor for controlling sensor's Lift-off distance.

A quadrature encoder sensor takes measurements of each step to ensure the stepper motor does not skip. The solenoid moves at a constant speed through a test to ensure the sensor measurements are smooth. A typical inspection moves the solenoid over a thirty centimeter scan. Figure 3.13 shows an experimental recording of encoder measurements versus time for a 70 centimeter inspection scan.

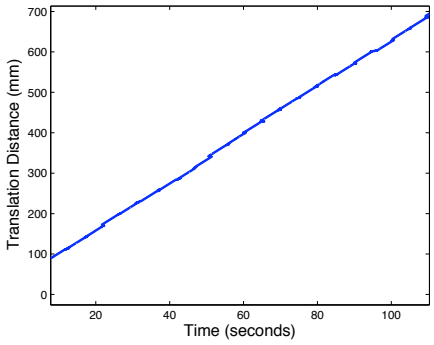

Figure 3.13: Translation Distance from 70 cm scan

3.2.3 Stepper Motors

The system has control electronics to drive the stepper motors and receive analog signals from the hall-effect sensors. The stepper motors are made by Superior Electric SLO-SYN and the harmonic gearbox (PSS050-020) is made by Harmonic Drive Technologies. The stepper motor electronics use a microstepping design [24] to achieve a greater resolution than the 200 steps per revolution alloted by the stepper motor. The electronic printed circuit board (PCB) is based off a 3-axis stepper motor control design by HobbyCNC [25]. The stepper motors are located in close proximity to the control electronics as shown in Figure 3.14 .

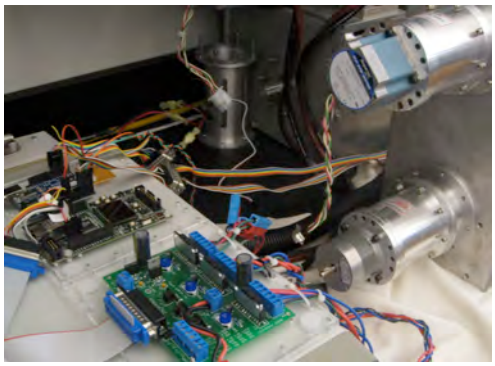

Figure 3.14: Control Electronics for MFL Solenoid and Stepper Motors

3.2.4 Labview Interface

A Labview interface is utilized to visualize data and communicate with the motors and sensor electronics. Labview is a graphical programming language used to develop sophisticated measurement, test, and control systems using a flowchart like programming environment. A user manipulates the Labview graphical interface shown in Figure 3.15 to initialize the test and collect data packet logs.

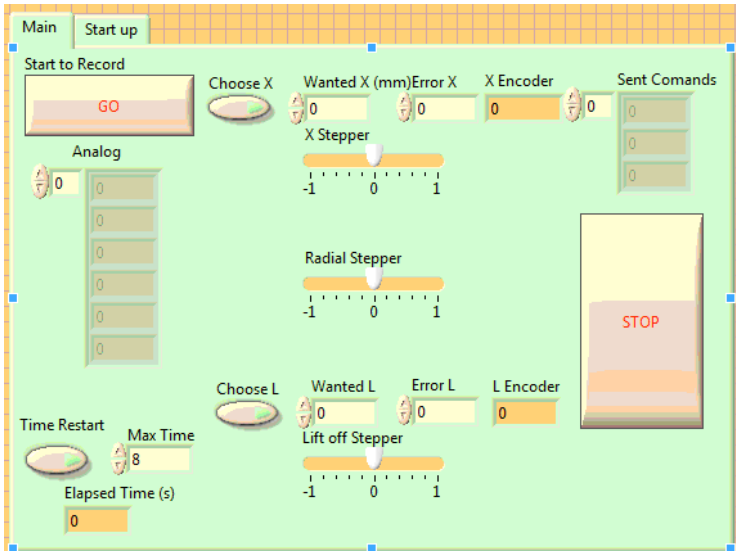

Figure 3.15: Labview Interface for Stepper Control and Hall-Effect Logging

3.2.5 Solenoid Motion Electronics

Operating the solenoid involves communicating with a microcontroller that relays the motor signals and feedback from the sensors. The logging and command system utilizes an Arduino microcontroller [26] for analog and digital measurement. Analog inputs connect to a three-axis Hall effect, voltage, and current sensors. The digital lines are configured to limit switches and encoders for position measurement.

The Arduino also has output pulse width modulation (PWM) capabilities for controlling the three axis stepper motor automation. Two of the three stepper motors have sensor feedback with quadrature encoders. The encoders are hardware interrupt based on the

microcontroller to allow for accurate positioning in the translation of the solenoid coil along the pipe.

The stepper motors receive power from chopper drive power control board based off a Hobby CNC design [25]. The stepper control board requires one PWM and digital signal for each motor. The PWM signal determines the speed of the stepper motor, and the digital signal determines the motor's direction. Therefore, three PWM pins and three digital output pins from the Arduino control the 3-axis stepper motor system. For further reference of the solenoid electronic components see Figure 3.16 and Appendix A.1.

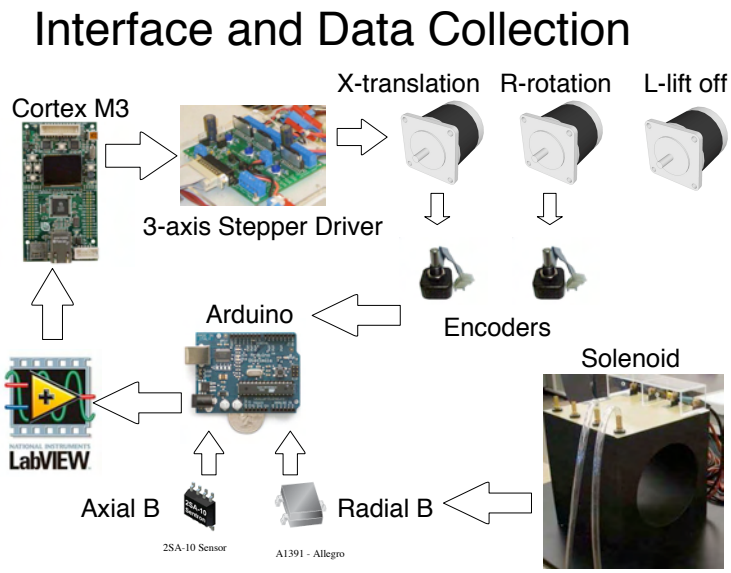

Figure 3.16: Microcontroller system for logging and controlling 3-axis stepper board.

3.3 Sensor

An integrated two-axis Hall-effect sensor (Sentron 2SA-10) and linear Hall-effect sensor (Allegro A132X family) are used to measure the radial and axial signals. Both sensors are attached to a small plastic plate. The sensor plate is mounted in the axial center of the

solenoid. The sensor's lift-off is equal to the width of the plastic enclosure touching the side of the pipe wall.

3.3.1 Lift-off Experiment

As shown by Schmitte, the lift-off is a vital factor in the quality of the signal [16]. As lift-off is increased, the signal amplitude decreases, and the shape of the curve becomes less defined. Because the curve's shape and extrema are used to locate and classify the defect, lift-off must be controlled and minimized. Experimental tests were conducted to show the effect of lift-off on the external MFL inspection device. Figure 3.17 illustrates a comparison of lift-off distance from the pipe wall over a set of two defects. The well defined peaks and ridges in sub-figure 3.17(a) increase detection quality. In external MFL, sub-millimeter lift-off enables detection of wall thinning defects of 5% or greater for pipe wall thickness of at least 4mm.

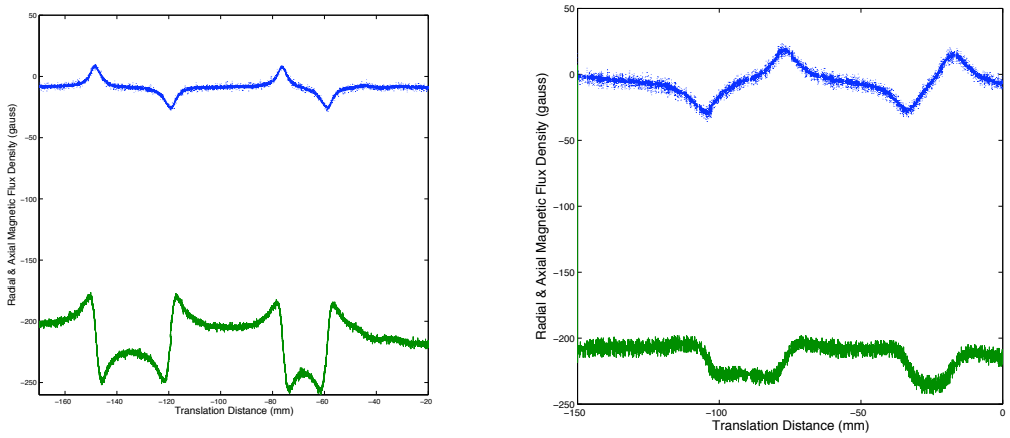

(a) Signal with normal lift-off

(b) Signal with increased lift-off

Figure 3.17: MFL signals for different lift-offs (Radial-Blue/Dotted , Axial-Green)

3.3.2 Sensor Enclosure

Tests of the dual-axis Hall-effect sensor were conducted with the sensor in different orientations, resulting in varied lift-offs. The lift-off differences on the signal quality is apparent in sub-figures 3.17(b) and 3.17(a). The distinct difference in definition and amplitude confirmed the importance of a small lift-off. Therefore, the custom sensor mount minimized the lift-off of the sensor while protecting the face of the sensor from contact with the pipe. The mounting structure, shown in Figure 3.18(a) is a two-part ABS-plastic enclosure to fit the Hall effect sensor and maintain a minimal lift-off without inflicting damage on the sensor surface.

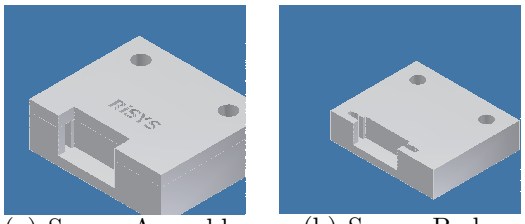

(a) Sensor Assembly (b) Sensor Body

Figure 3.18: Hall Effect Sensor Package Assembly and Body

The sensor mount module is a compact brick which mounts easily to an aluminum bar inside of the solenoid. It is intended to be modular to allow for additional sensors to be added or switched easily. The module is composed of two separate body and lid pieces. The compartment for the sensor plate is contained within the body. The lid is affixed to the top, as seen in Figure 3.18(a), to secure the sensor and prevent any vertical movement, which could alter the reading of the signal.

The sensor compartment is dimensioned to create a tight fit for the sensor plate, again to eliminate movement. The holes in the slot allow the sensor to be removed despite the tight fit. The slot is positioned to place the sensor at the magnetic center of the solenoid (Figure 3.19).

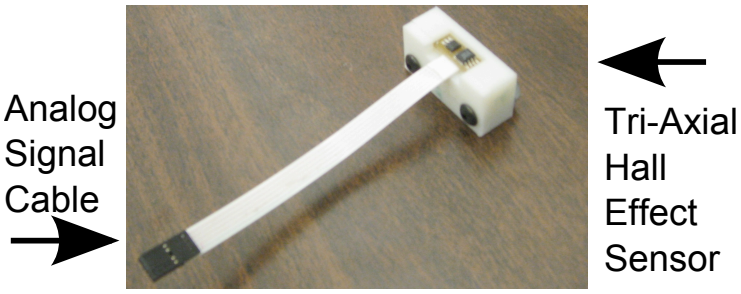

Figure 3.19: MFL Sensor with Tri-Axial Hall Effect sensor

Chapter 4

External and Internal Comparison

Magnetic flux leakage inspection has developed into a viable non-destructive evaluation technique for ferromagnetic structures. The early MFL testing platforms employed external field generation and external sensing from the test specimen. For pipe inspection, external MFL inspection is the primary method of obtaining defect information about a pipe structure. Recently, internal MFL inspection has arisen as a more advantageous method of sensing pipes especially when external sensing is not applicable. This chapter draws comparisons between internal and external magnetic flux leakage inspection methods. Experiments have been performed with both techniques. An overview of the experiment and method of each technique is presented to provide a baseline comparison.

4.1 Internal Inspection Experiment

An 18 foot continuous steel pipe with a 2.5 inch inner diameter was mounted rigidly and supported on the opposite end with steel cables as shown in Figure 4.1. The cantilevered pipe is opened on both ends to allow the MFL robot to travel through the pipe.

Figure 4.1: Steel pipe with PCTI Internal Robot mounted on the right

The MFL robot is designed for Pipeline Inspection Gauge (PIG) operations and typically propelled by fluid pressure in the pipe. For the purpose of the inspection tests, the MFL robot was outfitted to a custom winch to pull the robot through the cantilevered

pipe. The robot begins the experiment on the open end of the pipe as depicted in Figure 4.2 and traverses through the defected pipe and unmodified pipe in one complete data collection period.

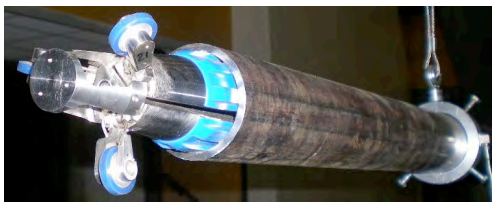

Figure 4.2: PCTI Internal Robot in 24 foot steel pipe

4.1.1 Internal Inspection Tests

Six precision wall thinning defects were utilized for the purpose of internal inspection tests. Defects were cut into two foot segments of pipe as shown in Figure 4.3 with two unique defects per segment. The defects are approximately 5 inches long. The three pipe segments were connected to the 18 foot pipe with PVC couplers to form a 24 foot pipe. The robot traversed through the six different defects to travel a total distance of 24 foot in one experiment log.

Figure 4.3: 2 foot Segment of Pipe

4.1.2 Overview of Internal Signals

Magnetic flux leakage signals involve an axial and radial component to properly characterize a defect. The magnetic flux density components are measured using hall effect sensors oriented in each respective axis. The radial magnetic flux density B_{rad} signal denotes the start and ending of a defect with the respective maximum and minimum peaks as shown

in Figure 4.4(a). The axial magnetic flux density represents the volume of loss material in the defect. For most inspection purposes, the axial signal is important to determining the geometry and severity of the defect. A clear axial signal has a well defined curved shape as shown in Figure 4.4(a).

In presenting data, the axial and radial signals are plotted in the same figure to denote a defect in the pipe structure. As in Figure 4.4(a), the data can be denoted in a two-axis plot (left) or a single axis for ease of visualization (right). The defect depicted is a 5 inch defect as shown in Figure 4.3 with a 30% wall thinning defect therefore the pipe wall has 70% of its normal thickness.

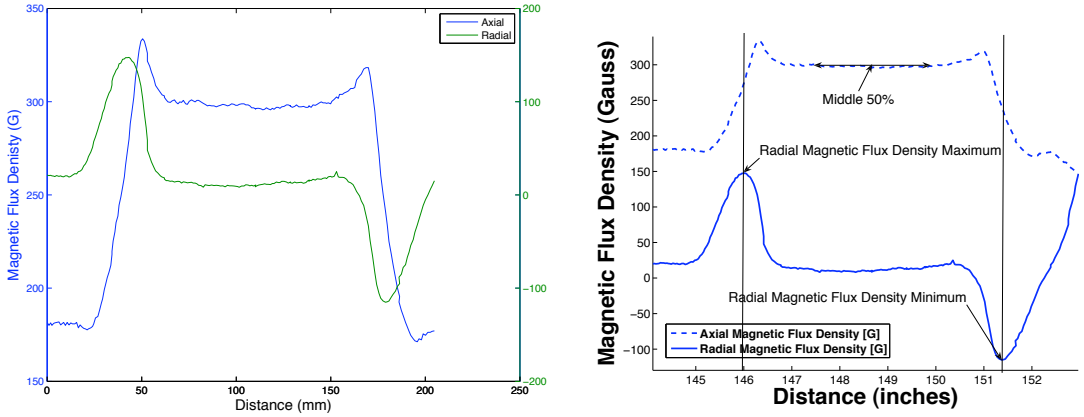

(a) Axial and Radial of 30% Defect

(b) Filtered Signal of 30% Defect

Figure 4.4: Axial and Radial plotted on different scales

A close-up view of each defect is shown in Figure 4.5 with two-axis plots for ease of visualization. The signals generated were measured with the MFL robot's Hall effect sensors. Data collection was performed on a single scan through the 24 foot pipe with defects. These figures show the radial and axial signals from the internal robot inspections of 5, 10, 15, 25, 30 and 60 % wall thinning defects.

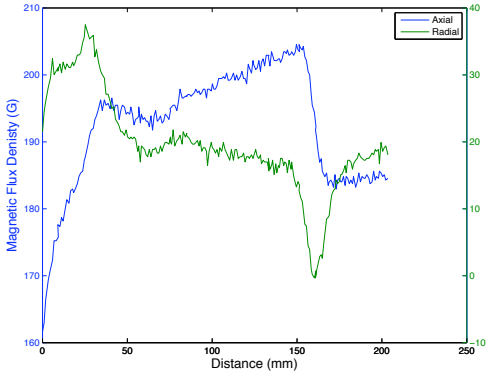

(a) 5% thinning

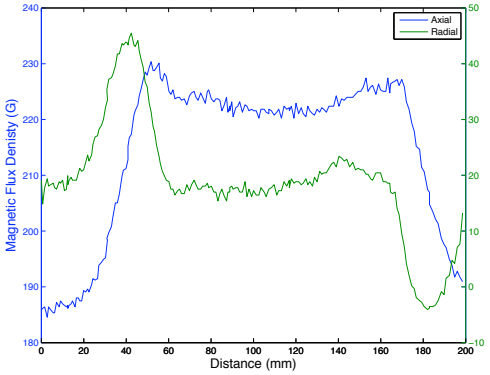

(b) 10% thinning

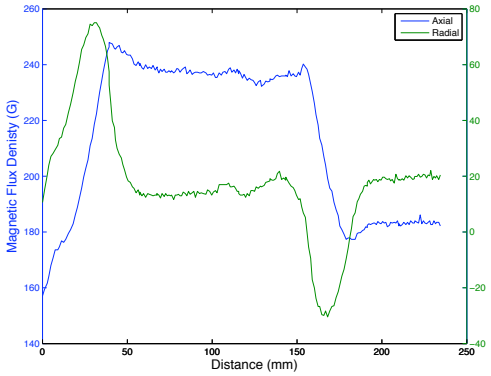

(c) 15% thinning

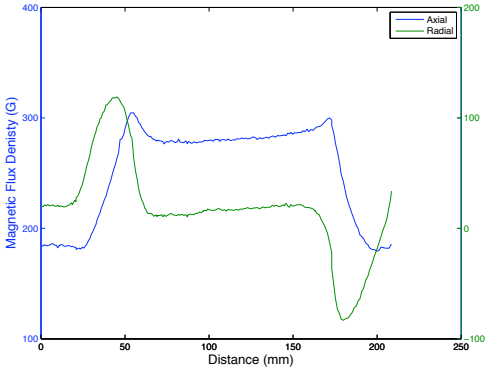

(d) 25% thinning

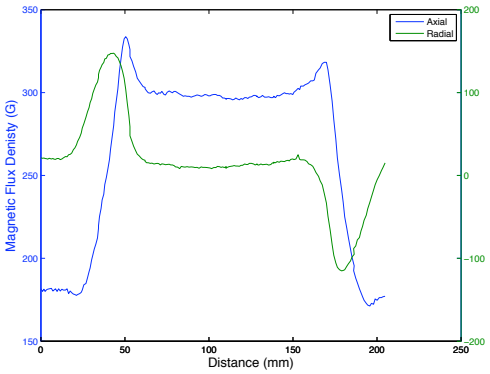

(e) 30% thinning

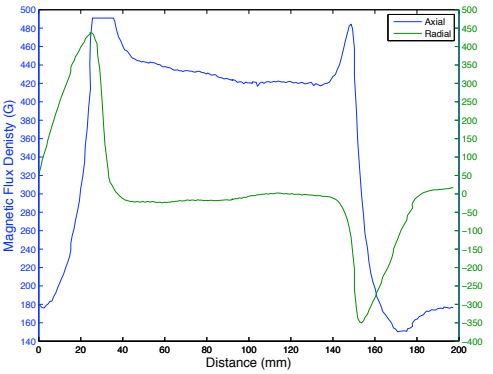

(f) 60% thinning

Figure 4.5: Raw magnetic flux signals from internal robot inspection.

4.2 External Inspection Experiment

For external inspection tests, the solenoid coil traverses a pipe specimen and monitors MFL signal perturbations. The pipe segment is a four foot steel pipe with a 2.5 inch inner diameter mounted with rigid cone supports on both sides. The segment is a combination of the two foot pipe sections as shown in previous Figure 4.3. The pipe can be rotated by a stepper motor while the solenoid is translated by a separate stepper motor harmonic drive system. The complete pipe support and solenoid are configured as in Figure 4.6.

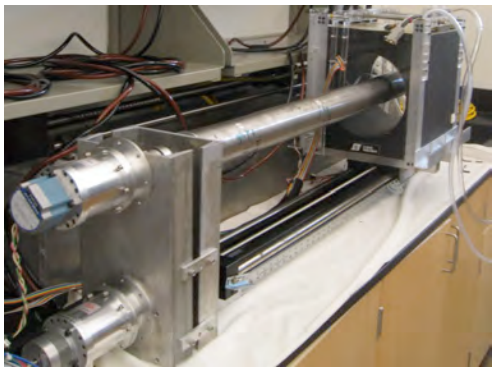

Figure 4.6: MFL Solenoid and 4-Foot Pipe Structure

The MFL sensor package records analog signals corresponding to the axial magnetic flux density. For the purpose of the inspection tests, the MFL external inspection coil moves at a slow speed to produce accurate readings. The MFL solenoid coil starts the experiment on a non-defected part of the pipe and makes a 30 cm scan across any defects that are present on the pipe.

4.2.1 External Inspection Tests

Similar to internal inspection, six different wall thinning defects of 5, 10, 15, 25, 30 and 60 percent were analyzed by the MFL external inspection experiment. Defects are segmented into two foot sections of pipe and connected together to form a four foot section to analyze with the MFL solenoid coil. Due to sheer volume of data, the solenoid coil collects one

five inch defect at a time in a thirty centimeter scan. The radial and axial signals from the external robot inspections are shown in Figure 4.7.

4.3 Internal and External Data

Internal and external MFL signals are plotted jointly on the one axis to draw comparisons between the two inspection techniques. The magnetic flux signals are compared in Figure 4.8 to delineate difference in radial and axial signals for 5% to 60% defects.

4.3.1 Inspection Technique Similarities

The internal and external data draw many correlations which provide a foundation for analysis between the two sensing methods. Internal is a more difficult technology to implement due to dimension constraints and environment conditions, therefore external MFL sensing is a beneficial enhancement tool to internal inspection design. Both methods show accurate detection of wall thinning defects from 5% to 60% for MFL pipe inspection. Since both methods use the same hall-effect sensors, the sensor analog voltage sensor noise is similar. One method to improve analog noise is to increase resolution of an analog to digital converter. Another approach is to remove analog and utilize a digital Hall effect sensor. However, at present time only analog linear Hall effect sensors are availble on the market [27].

Internal and external inspection tests show comparable radial MFL signals. The amplitude of the radial data is noticeably dissimilar for large wall thinning defects. However the amplitude of the radial MFL signal is of lesser importance than the position of the radial peaks. The peak of the maximum or minimum represents the beginning of the defect. The spacing between the radial peaks denote the length of the defect along the axis of the pipe. The radial spacing between the two MFL techniques are approximately equivalent.

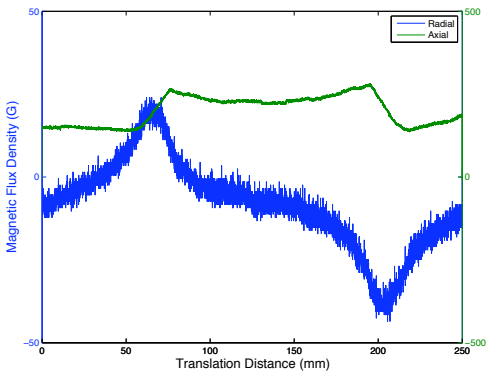

(a) 5% thinning

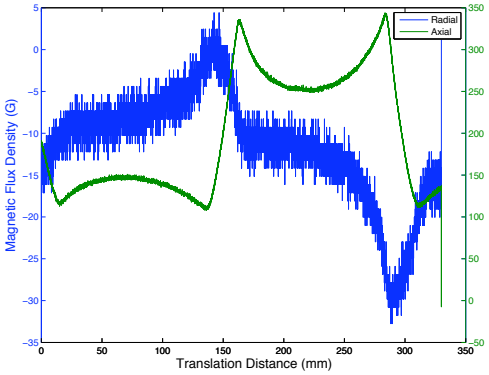

(b) 10% thinning

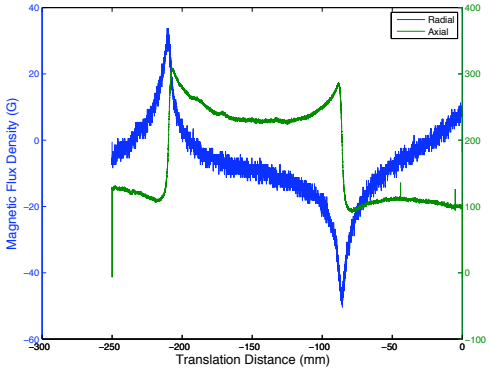

(c) 15% thinning

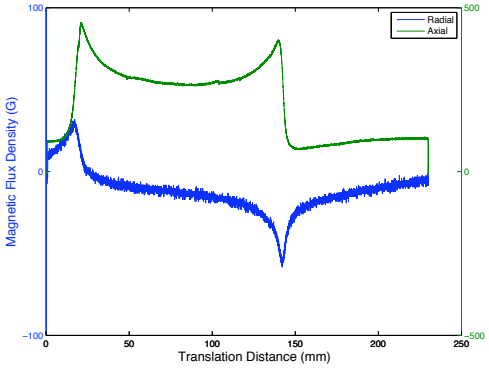

(d) 25% thinning

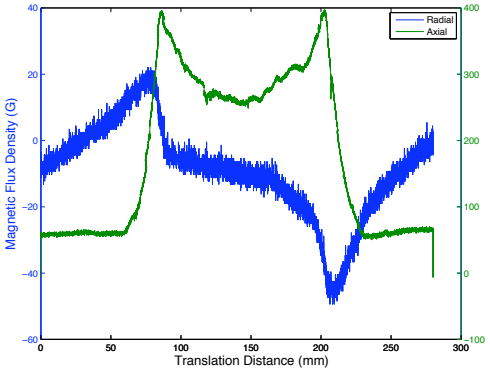

(e) 30% thinning

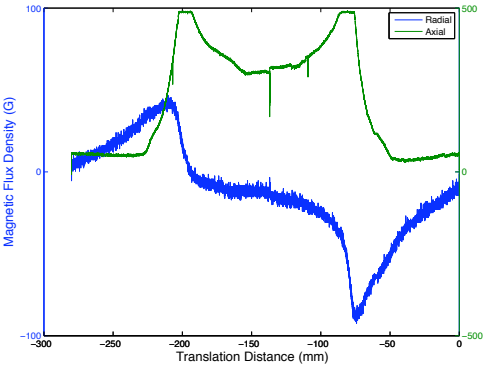

(f) 60% thinning

Figure 4.7: Raw magnetic flux signals from external robot inspection.

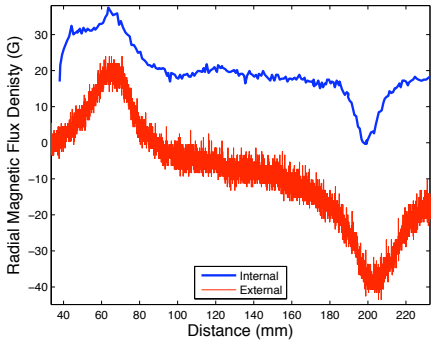

(a) 5% thinning - Radial

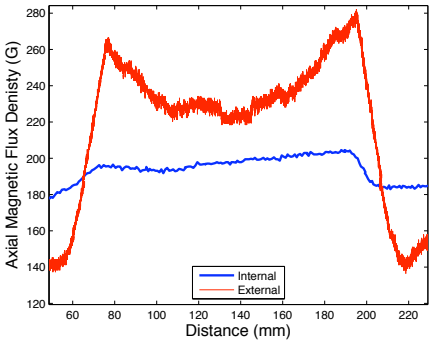

(b) 5% thinning - Axial

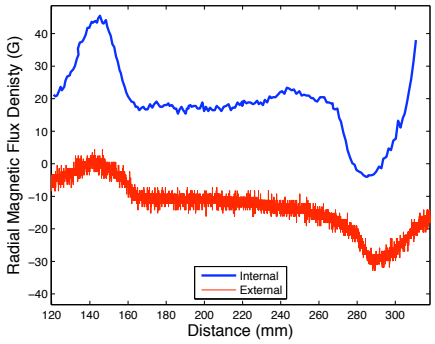

(c) 10% thinning - Radial

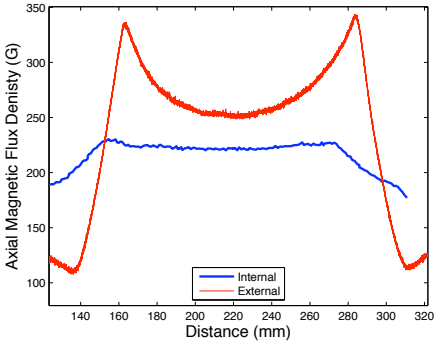

(d) 10% thinning - Axial

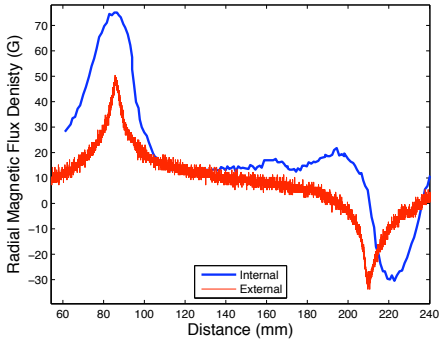

(e) 15% thinning - Radial

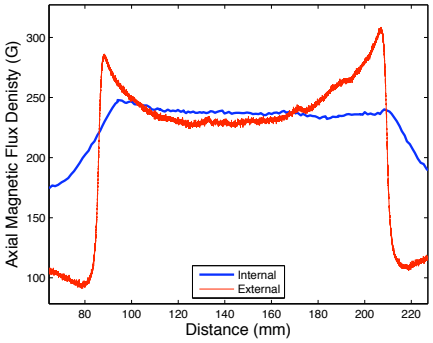

(f) 15% thinning - Axial

Figure 4.8: Magnetic flux signal for external and internal robot inspection. (5,10,15%)

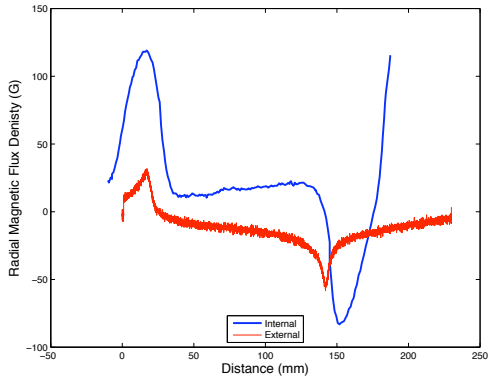

(a) 25% thinning - Radial

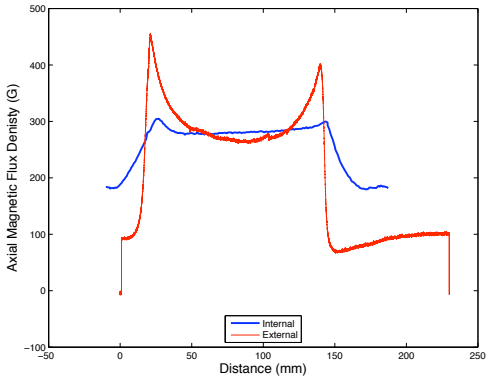

(b) 25% thinning - Axial

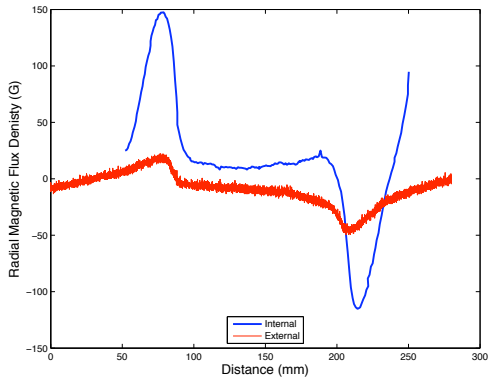

(c) 30% thinning - Radial

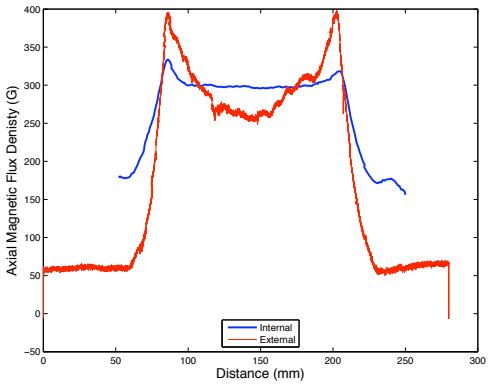

(d) 30% thinning - Axial

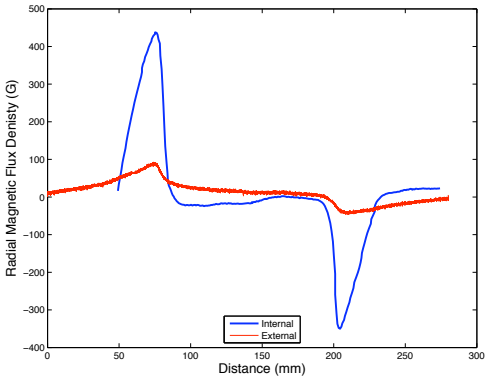

(e) 60% thinning - Radial

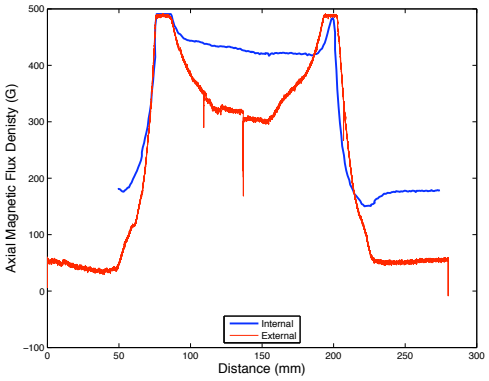

(f) 60% thinning - Axial

Figure 4.9: Magnetic flux signal for external and internal robot inspection. (25,30,60%)

4.3.2 Inspection Technique Differences

Internal and external inspection techniques are fundamentally different because of the location of the sensors and generation of the field. Internal inspection has a large number of constraints to the size of the inner pipe diameter. Small pipe dimensions create havoc when integrating permanent magnets, electronics and sensor suite. On the other hand, external inspection is more flexible with power constraints, coil dimensions and sensor placement. These external electromagnetic apparatus variations enable control of the magnetic field characteristics. External inspection also has the advantage of using stepper motors and high precision harmonic drives to obtain accurate positioning. A portion of the noise in internal inspection MFL signals can be attributed to sparse distance measurements.

The external solenoid coil provides the option of generating a time-varying magnetic field. Internal inspection generates a static field with a fixed permanent magnets. When running tests, the external inspection system has the potential to have power variations in field generation that lead to noise spikes in the baseline magnetic field signal.

From 5% Axial comparisons (Figure 4.8(b)), external inspection exhibits more sensitivity for small wall thinning defects. External MFL signals also show well defined curvature for 10% and 15% wall thinning defects. As the defect grows larger past 30%, the differences in external and internal MFL inspection signals are less significant.

In terms of coil tubing (CT) technology, the external solenoid shows significant advantage in producing a larger uniform axial regions. Coil tubing wall thickness measurements require a highly uniform longitudinal magnetic field to detect transverse flaws [12].

Chapter 5

MFL Inspection Analysis

This section covers the significant contributions to the field of MFL inspection techniques. A relation between internal and external inspection is presented to offer a baseline test method to understand inspection techniques.

5.1 Internal and External Generalization

Magnetic flux leakage inspection can be separated into internal and external techniques. In the context of these experiments, external inspection is a baseline method to measure performance against internal systems. The external MFL solenoid coil experimentation opens design boundaries of internal MFL inspection systems.

5.2 Defect Processing

The Defect Locater and Axial Averaging (DLAA) algorithm uses the maxima and minima of the radial magnetic flux data to identify defects and find the relative average of corresponding axial data. The process of the algorithm begins with a moving average filter to minimize radial signal noise. Then, the maxima and minima of the radial magnetic flux data are calculated with derivatives to denote the position of the defects on a pipe. A maximum represents the start of a defect, while a minimum signals the end of the defect. Using the start and ending points of the defects, the relative mean of the axial magnetic flux data is determined for each defect. Finally, a wall thinning curve is produced by relating the computed averages for each defect and the corresponding wall thickness.

5.2.1 Filtered and Raw Data

The raw data, as seen in Figure 5.1, has noise and needs to be filtered before processing. To minimize the effect of noise, an extended moving average filter was used on the radial data prior to locating minima and maxima.

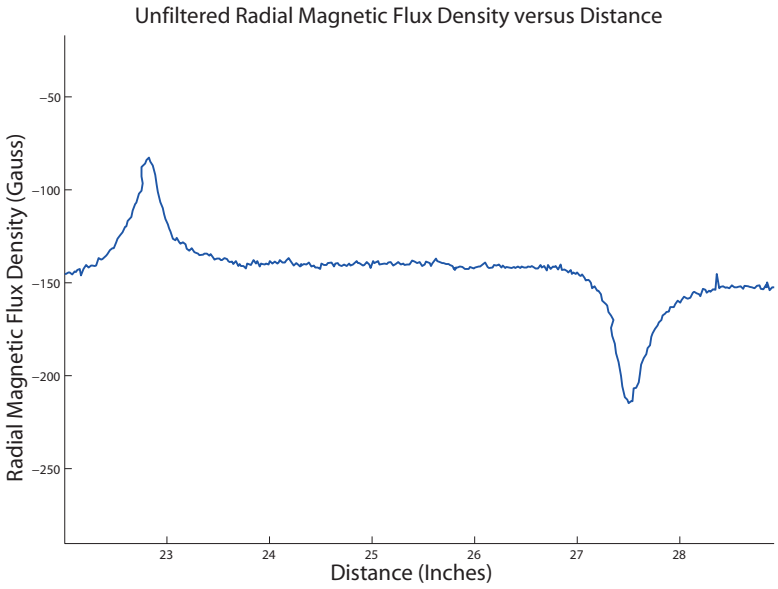

Figure 5.1: Radial MFL Signal from a Internal Inspection 30% defect.

5.2.2 Finding Minima and Maxima

After the extended moving average filter is used, the difference between each of the radial magnetic flux values is computed and stored. If the difference is less than calibrated noise cut-off (0.5 G), then the difference is factored out. Sign changes in the differences are used to find radial min-max pairs which denotes the location of a defect. After using the extended moving average filter, no extraneous minima or maxima are found, as shown in Figure 5.3.

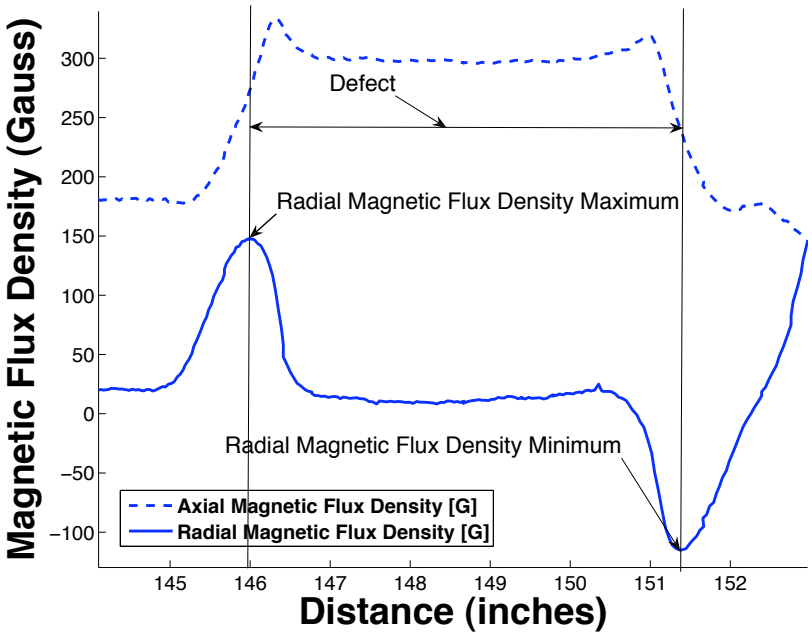

Figure 5.2: The defect is located between the maxima and minima of the radial data.

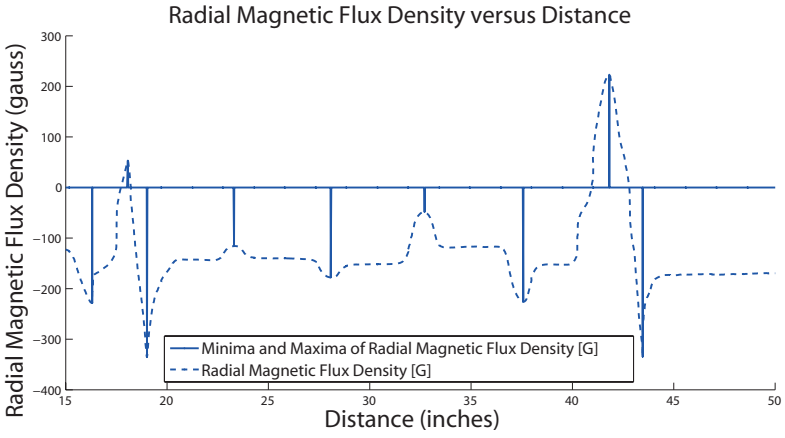

Figure 5.3: Filtered Radial Magnetic Flux Density of multiple wall thinnings with minima and maxima denoted. Only necessary minima and maxima are detected after using extended moving average filter.

5.2.3 Axial Averaging

An estimate of wall thickness is obtained by averaging the middle 50% of the axial magnetic flux values for each defect. The middle 50% is calculated based on radial magnetic flux maxima-minima pairs as distance bounds as shown in Figure 5.4.

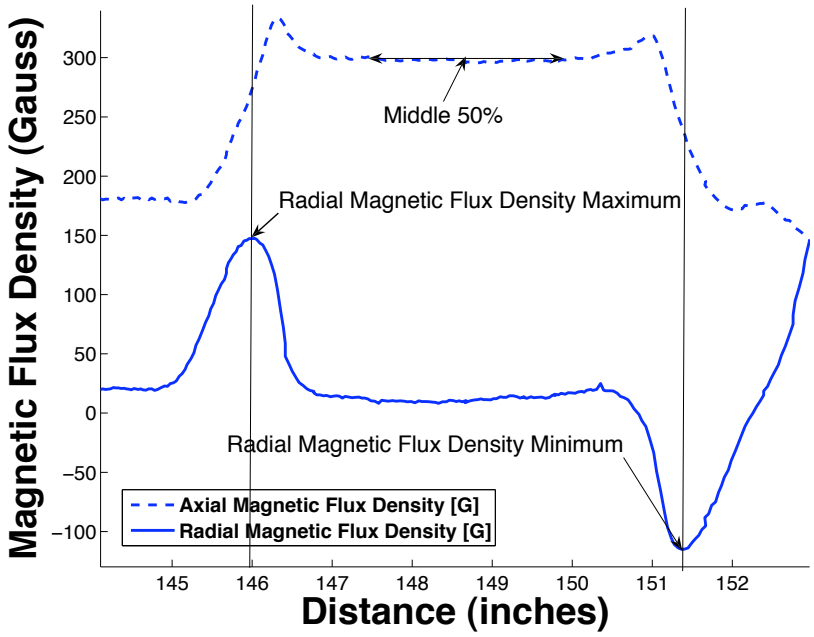

Figure 5.4: The minima and maxima of the filtered Radial Magnetic Flux Data are used to locate the defect, as shown with a 30% wall thinning.

The vertical lines indicate the maximum and minimum on the radial magnetic flux data and the corresponding location on the axial magnetic flux data. The middle 50% of the axial magnetic flux data between these points is given relative average according to the baseline MFL signal. The axial magnetic flux averages of each defect can be grouped into patterns to inverse identification of wall thickness.

5.2.4 Wall Thickness Curves

Each defect will undergo a series of signal processing techniques as described in Section 5.2. The defect's averaged axial MFL estimate provides an experimental data point. These averaged axial values are plotted against the true wall thickness of each defect. For the internal inspection tests, the radial maximum-minimum pairs are crucial to locate multiple defects in a scan of the internal robot. The defect search algorithm has a noise cancellation component to filter out smaller local peaks. Once a maximum-minimum pair is located for a defect, the axial averaged estimate of magnetic flux density can be referenced against a previously known wall thickness. Figure 5.5 shows a plot of all averaged axial magnetic flux points versus percentage wall thickness values for the internal robot inspection tests.

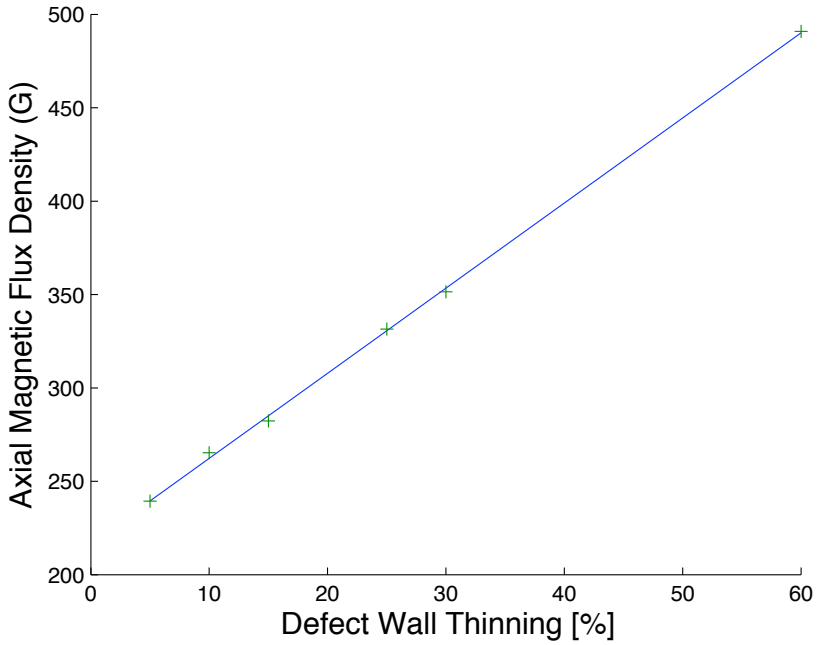

Figure 5.5: Average axial MFL signals versus Actual Wall Thinning % Sizes for Internal MFL Robot. Linear regression applied to six data points.

The internal MFL estimation curve provides an approximate guideline from 5% to 60% wall thinning defects. The estimation was obtained with least squares linear regression fit. Future work with more unique defects has the potential to extend this work to a curve fit

for all types of wall thinning defects.

The external inspection tests were also processed using the same procedure as detailed to generate a series of wall thinning curves. The solenoid inspection tests are measuring from a different baseline axial MFL signals than the internal robot's permanent magnetic field. The relative axial averaging compensates for the difference in baseline signals and produces similar wall thinning curves to the internal inspection tests as shown in Figure 5.6.

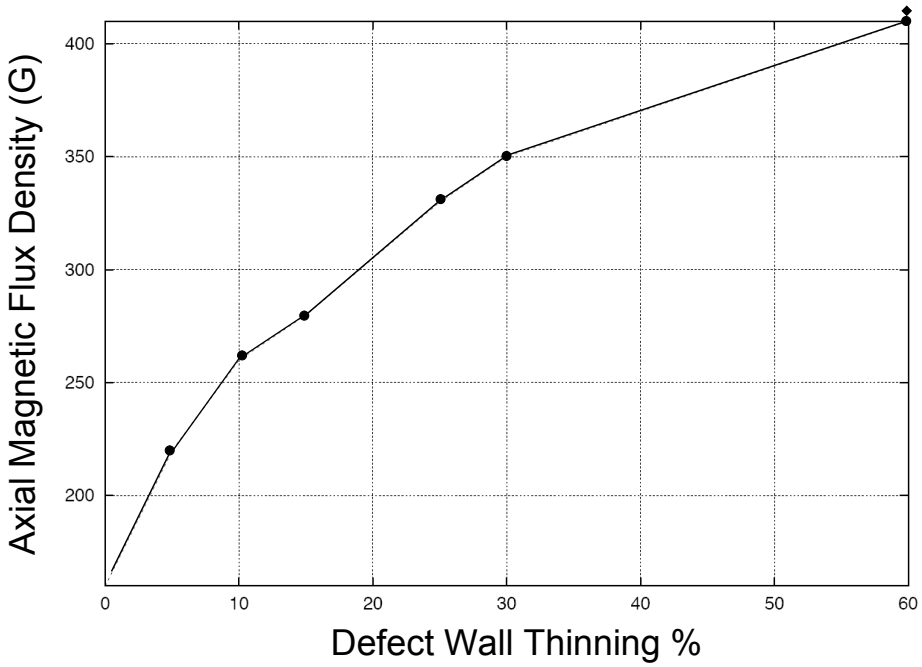

Figure 5.6: Average axial MFL signals versus Actual Wall Thinning % Defects for External Inspection tests.

The external and internal wall thinning curves differ due to field characteristics and testing procedures. The internal inspection tests are able to collect all pipe wall defects in one scan to form a cohesive data set for processing. The solenoid data processing of multiple defects has more parameters due to pipe length constraints. The solenoid inspection table is only able to monitor two 5 inch defects in one scan due to the dimensions of the 2 foot pipe segments in a 4 foot space.

5.3 MFL Inspection Improvements

Magnetic flux leakage inspection can be improved with more accurate sensors and defect geometry models. The 5 and 10 % wall thinning defects from Figure 4.5(b) show a noisy MFL signal. With a certain threshold of noise, the radial MFL signals are difficult to process even with sufficent filtering. Potential improvements to measuring small defects with Internal Robots involve magnetic field resolution and spatial resolution.

5.3.1 Internal Robot - Signal to Noise

The six unique wall thinning defects present a wide spectrum of potential defects. Figure 4.5(f) plots a large defect and shows a significantly higher quality signal relative to noise. In addition, the Axial signal shape becomes more pronounced with a defining trapezoidal shape as wall thinning defect size increases. The 5% and 10% defects are more difficult to recognize. The Robot uses a 16-bit analog to digital converter which produces very high quality raw signals. The upper-end analog to digital converter can achieve 24-bits but sensor noise constraints might be the more important issue. The Hall effect sensor resolution and noise are not well defined for linear Hall effect sensors and need further understanding.

5.3.2 Increasing Resolution

Increasing resolution in Hall effect sensors will greatly improve the observed noise in experimental MFL data. Linear hall effect sensors can shift sensitivity in the voltage V per Gauss G to enhance resolution of the MFL measurements. Small wall thinning defects need the best possible resolution to differentiate the signal from noise. The signal to noise ratio difference is very apparent between 5% defect 5.7(a) and a 60% wall thinning defect 5.7(b). In addition, reducing lift-off distance dramatically improves axial field stregnth signal quality [3].

Another potential way to improve signal quality involves the distance measurement

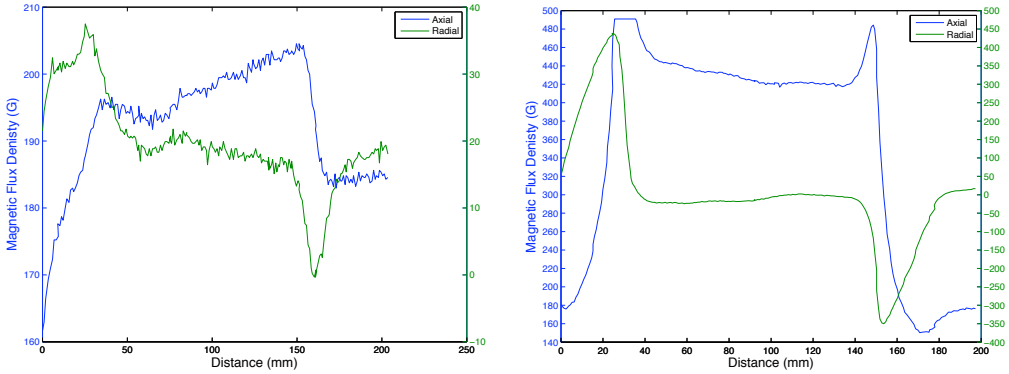

(a) 5% thinning (b) 60% thinning

Figure 5.7: Comparison of 5% and 60% Internal Robot Measurements

resolution. The spatial distance resolution is based off the resolution of the quadrature encoder. Encoder wheels are the primary method of recording distance measurements in internal inspection. Encoder wheel slippage is a significant issue because the robot's position accuracy will drift over time. Adding a second wheel/encoder follower with a different friction surface will increase the overall robot's spatial measurement reliability. Increasing quadrature encoder resolution with higher quality rotary encoders is also an effective method to improve spatial measurements.

5.4 Conclusion

MFL testing has become into an important method for inspection of pipelines and tubing in order to prevent long-term failures. Industry relies on MFL as a simple binary inspection indicator without consideration of defect geometry or severity. This work presented an experimental solenoid coil for external MFL robotic inspection and a series of tests with an internal MFL robot. Enhancements have been shown to improve magnetic flux leakage inspection device design and signal analysis. This thesis compared the experimental solenoid and an internal MFL pipe robotic device in the non-destructive evaluation (NDE) of a ferromagnetic pipeline. The unique contributions in internal and external magnetic

flux leakage inspection revolve around experimentation and analysis. The first contribution provided insight into internal inspection with a commercial robotics inspection device. In addition, an external solenoid device created specifically for MFL research has demonstrated uniform magnetic field generation and suitable MFL performance results with wall thinning defects.

Bibliography

[1] C. FlatPack, "T-rock coiled tubing truck performing a cleanout." available at `http://www.cjsflatpack.ca`, 2009.

[2] J. Nestleroth and T. Bubenik, "Magnetic flux leakage technology for natural gas pipeline inspection," tech. rep., Battelle for The Gas Research Institute, February 1999.

[3] S. M. Dutta, *Magnetic flux leakage sensing: the forward and inverse problems*. PhD thesis, Rice University, 2008.

[4] N. O. Varco, "qt 1000 product datasheet." available at `http://www.nov.com`, 2009.

[5] D. Akilla, "Analysis of magnetic flux leakage signals for surface defects in coiled tubing," Master's thesis, Tulsa University, 2004.

[6] S. M. Tipton and D. A. Newburn, "Monitoring coiled tubing fatigue life," in *Second International Conference on Coiled Tubing Operations*, (Houston, TX), pp. 28–31, Gulf Publishing Company and World Oil, March 1994.

[7] A. R. 5C8, "Recommended practice for care, maintenance and inspection of coiled tubular product," tech. rep., Draft 7 Rev. 3, November 2004.

[8] H. Haines, T. Bubenik, and J. Nestleroth, "Characterization of magnetic flux leakage (mfl) indication found during inline inspection of natural gas transmission pipelines," tech. rep., Gas Research Institute, July 1995.

[9] S. Mandayam, L. Udpa, S. S. Udpa1, and W. Lord, "Signal processing for in-line inspection of gas transmission pipelines," *Research in Nondestructive Evaluation*, vol. 8, pp. 1432–2110, July 2006.

[10] W. Lord and D. Oswald, "Leakage field methods of defect detection," *International Journal of Nondestructive Testing*, vol. 4, p. 249, 1972.

[11] J. Haueisen, R. Unger, and M. E. Bellemann, "Evaluation of inverse algorithms in the analysis of magnetic flux leakage data," *IEEE Transactions on Magnetics*, vol. 38, pp. 1481–1488, May 2002.

[12] R. K. Stanley, "Some new developments applicable to coiled tubulars," in *Coiled Tubing Conference*, (Houston, TX), p. SPE Paper No. 94058, SPE/ICoTA, 2005.

[13] P. Ivanov, Z. Zhang, C. Yeoh, L. Udpa, Y. Sun, S. Udpa, and W. Lord, "Magnetic flux leakage modeling for mechanical damage in trasmission pipelines," *IEEE Transactions on Magnetics*, vol. 34, pp. 3020–3, September 1998.

[14] Y. Li, J. Wilson, and G. Tian, "Experiment and simulation study of 3d magnetic field sensing for defect characterisation," *NDT & E International*, vol. 40, pp. 179–184, 2007.

[15] D. Atherton and M. Daly, "Finite element calculation of magnetic flux leakage detector signals," *NDT International*, vol. 20, pp. 235–8, August 1987.

[16] T. Schmitte and S. Nitsche, "Modeling of magnetic flux leakage measurements of steel pipes." European Conference on Non-Destructive Testing, 2006.

[17] E. Altschuler and A. Pignotti, "Nonlinear model of flaw detection in steel pipes by magnetic flux leakage," *NDT & E International*, vol. 28, no. 1, pp. 35–40, 1995.

[18] K. Mandal and D. L. Atherton, "A study of magnetic flux-leakage signals," *J. Phys. D: Appl. Phys.*, vol. 31, pp. 3211–3217, July 1998.

[19] M. Afzal and S. Udpa, "Advanced signal processing of magnetic flux leakage data obtained from seamless gas pipeline," *NDT and E International*, vol. 35, no. 7, pp. 449–457, 2002.

[20] J. Nestleroth and A. Crouch, "Variation of magnetic properties in pipeline steels," Tech. Rep. Report No. DTRS56-96-C-0010, U.S. Dept. of Transportation, March 1998.

[21] D. Bray and R. Stanley, *Nondestructive Evaluation: A Tool in Design, Manufacturing, and Service*. CRC Press, 1984.

[22] C. Edwards and S. Palmer, "The magnetic leakage field of surface-breaking cracks," *Journal of Physics D: Applied Physics*, vol. 19, pp. 657–673, 1986.

[23] M. T. H. R. L. Elbaile and R. Iglesias, "External fields created by uniformly magnetized ellipsoids and spheroids," *IEEE Transactions on Magnetics*, vol. 31(1), pp. 830–836, January 1995.

[24] L. W. Hunter, "Microstepping motor controller circuit," ., March 1988. US Patent 4734847.

[25] D. Rigotti, "Hobbycnc pro chopper driver board kit." available at `http://www.hobbycnc.com/`, 2009.

[26] Gravitech, "Arduino specifications and reference documents." available at `http://www.arduino.cc`, 2009.

[27] A. MicroSystems, "Hall effect sensor catalog." available at `http://www.allegromicro.com/en/`, 2009.

Appendix A

Appendix

A.1 Solenoid Electronics

The Arduino Duemilanove is an open-source prototyping electronics board designed to be flexible with a simplistic programming environment [1]. The micro-controller has six 5 volt 10 bit analog input/output pins, 2 external interrupts, 5 PWM outputs, and 5 digital input/output pins. Although the PWM and interrupt pins are specialized, they can be used as a general purpose digital input/output. Additionally, the USB connector programs, powers, and serially connects the board to the computer. See Figure A.1 for a visual of the Arduino.

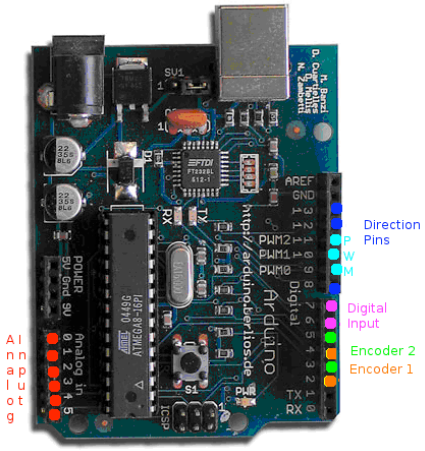

Figure A.1: Arduino microController with interfaces

A.1.1 Microcontroller Interfaces

The External MFL inspection system utilizes the Arduino microcontroller for analog and encoder measurement. The Arduino also relays PWMS signals the stepper motor positioning of the solenoid coil. The analog inputs connect to a three-axis Hall effect, voltage, and current sensors. The analog measurements were fairly stable with minimal bleed-over between analog channels. The system has three stepper motors, and therefore, three different moving parts that should be monitored with quadrature encoders. Quadrature

encoders connect to two digital input pins. One of the two pins must be a hardware interrupt, and the other pin is typically a general purpose digital input pin. Because encoders return either a high or low voltage, rather than an analog value, the Arduino will count the number of high/low encoder pulses. To keep track of the pulses, an interrupt calls a specific function when an encoder pulse is sent to the connecting pin. The Arduino only has two hardware interrupts; therefore that limits the controller to two encoders for 2-axis stepper movements. A software interrupt (PCINT) is potentially possible to allow for three simultaneous encoders. Therefore, encoders were mainly used on the two most important stepper motors.

A.1.2 Stepper Motor Control

The stepper motors are connected to a stepper power control board made by Hobby CNC [25]. The stepper control board requires one PWM and digital signal for each motor. The PWM signal determines the speed of the stepper motor, and the digital signal determines the motor's direction. Therefore, three PWM pins and three digital output pins from the Arduino control the 3-axis stepper motor system. To determine the proper frequency for the stepper motors, a function generator generated PWM signals to the stepper power control board. Using a square wave (50% duty cycle), a frequency from 2500 Hertz to 100 Hertz demonstrated which PWM frequencies controlled the stepper motor continuously. An oscilloscope helped measure the most ideal frequency (1429 hertz) for controlling the 3-axis stepper system. The Arduino frequency can be set to either 1381 or 976 Hertz [26], which was within range of 1429 Hertz to allow for proper stepper motor operation. The stepper motors are controlled by a serial port connection to a computer. Single ASCII character commands control the direction of each of the three stepper motors. For further reference of the ASCII stepper command characters, see Table A.1.

Stepper	Backward	Stop	Forward
Translation	w	x	y
Rotation	q	r	s
Lift-off	k	l	m

Table A.1: ASCII Character Serial Command

All of the stepper motors operate at the same speed and duty cycle ramping is not supported. The backward command is always one ASCII hexadecimal value minus the stop character command, and the forward command is always one plus the stop command. The character command pattern enabled simple serial codes for operation of the stepper motors. The Arduino system has the capability to add additional sensors in the future. The Arduino code can record and log additional analog and 2 digital pins. In the future, switches might be added to gain more information about the position of the lift-off sensor.

The overall Arduino system is setup to send PWM signals to stepper motors with encoder feedback and log a wide array of analog sensors.

A.1.3 Serial port and packet structure

The Arduino has to be able to store the data received in order for the data to be analyzed. The data includes the timer count, analog values, encoder values, and digital values. Some options would be to store the information on EEPROM, an SD card, or to send the data over the serial port to be stored by a PC computer. The EEPROM on the Arduino ATmel328 is 1 Kilobyte. The system takes over thirty minutes to complete one test, at 1 packet every 10 milliseconds, the amount of data to be stored quickly grows to 20 Megabytes in a single test. SD cards realtime storage is a potential solution, but SD cards have slow write cycle and limited capacity (less than 8GB). A computer connected over the USB cable can transfer data at 500 MB/sec with a large storage capacity. There are two ways the data could be sent, as characters to be readable by a human, or binary format for a computer. The problem with a program reading ASCII characters for data is that numbers can take up any amount of character spaces, and a program might not be able to distinguish where one number ends, and another begins. The ASCII character problem is alleviated when the data is sent in byte format. However, bytes are difficult to debug in a terminal program. Therefore, the strategy chosen for the Arduino communication electronics is to have both ASCII and byte versions with user select options.
If the ASCII character 'a' is chosen at the start of the program, then the program continuously sends an ASCII string over the serial port every 10 milliseconds. The time of 10 milliseconds was chosen based of the size of the data to send and the speed of serial communication 115,200 baud (roughly 3 milliseconds serial loop). These values were experimentally determined by triggering a digital output before the data had sent, and off once the data had finished sending. The digital signal was probed with an oscilloscope to measure the data packet timing. The string of data always starts with 'b' to signal the start of the data packet. The 'b' is followed by the time stamp, analog values, the two encoder values, two digital input values, a check sum, and an 'e' at the end all separated by commas. A sample line of data is presented in Figure A.2.

b,23,502,515,513,0,0,0,0,4,0,0,1557e

Table A.2: Sample Serial String

The string ends with a line return to represent the start of new data data. Line returns make enables clear formatting on a terminal screen. When 'b' is sent over the serial port, the Arduino sends back a packet in byte format. The Arduino's developing environment does not support sending data types (such as double and int), so instead the variables are broken up into bytes using bitwise AND and shift operations using the 'char' variable

type. The char variable is sent over the serial port as a "BYTE". An example of the data being sent is seen in Figure A.2.

```
hB = (encoder0Pos & 0xFF000000)>>24;
hmB = (encoder0Pos & 0x00FF0000)>>16;
lmB = (encoder0Pos & 0x0000FF00)>>8;
lB = encoder0Pos & 0x000000FF;
Serial.print(hB, BYTE);
Serial.print(hmB, BYTE);
Serial.print(lmB, BYTE);
Serial.print(lB, BYTE);
```

Figure A.2: Printing of BYTES on Serial Port

All parts of the variable are sent over, with the highest byte first. The pieces of each variable type are expected to be put back together in the receiving code. The data sent over the serial port is 's' to signify the beginning of the data packet. Similar to the data packet before, a four byte time stamp, 6 two byte analog values, 2 four byte analog values, 2 one byte digital values, and a four byte check sum at the end will be sent. To see a visual representation, see Table A.3.

DataType	1 Byte
Time Stamp	4 Bytes
Analog 0	2 Bytes
Analog 1	2 Bytes
Analog 2	2 Bytes
Analog 3	2 Bytes
Analog 4	2 Bytes
Analog 5	2 Bytes
Encoder 0	4 Bytes
Encoder 1	4 Bytes
Digital 0	1 Byte
Digital 1	1 Byte
Check Sum	4 Bytes

Table A.3: Serial Byte Packet Structure

The receiving program verifies the check sum to by adding all the variable bytes including the timestamp. If the checksum does not compute, than that packet of data will not be used. The packet structure is the foundation for the Arduino's data logging and communication capabilities.